Biomedical Signal Processing and Control 113 (2026) 109243

Contents lists available at ScienceDirect

Biomedical Signal Processing and Control

journal homepage: www.elsevier.com/locate/bspc

Stage-specific neurovascular complexity disruption in Alzheimer's spectrum: A resting-state fNIRS study using HFD, spectral and wavelet entropy

Min-Kyoung Kang [a], Keum-Shik Hong [a,b,*], Yong-Il Shin [c], Guanghao Huang [b]

[a] School of Mechanical Engineering, Pusan National University, 2 Busandaehak-ro, Geumjeong-gu, Busan 46241, South Korea
[b] Institute For Future, School of Automation, Qingdao University, Qingdao 266071, China
[c] Department of Rehabilitation Medicine, Pusan National University School of Medicine, Pusan National University Yangsan Hospital, Yangsan-si 50612, South Korea

ARTICLE INFO

Keywords:
Alzheimer's disease
Mild cognitive impairment
fNIRS
Fractal dimension
Spectral entropy
Resting-state neuroimaging

ABSTRACT

Early and noninvasive detection of Alzheimer's disease (AD) and its prodromal stage, mild cognitive impairment (MCI), is critical for timely intervention. This study introduces a stage-specific framework that integrates nonlinear complexity metrics—Higuchi's fractal dimension, spectral entropy, and wavelet entropy—applied to resting-state functional near-infrared spectroscopy (fNIRS) signals. fNIRS data were recorded from the prefrontal cortex of 83 individuals (AD: 19, MCI: 37, healthy controls (HC): 27), and complexity features were systematically analyzed across hemoglobin species.

HFD values declined progressively from HC to MCI to AD, whereas *SE* and *WE* increased in AD, reflecting altered signal irregularity. Intersection analysis identified a robust biomarker in the right frontopolar prefrontal cortex (channel 12), consistently discriminative across features and hemoglobin types. Classifiers trained on these core features outperformed full-channel models, achieving an AUC of 0.889 with low variability across folds. Complexity features also correlated strongly with Mini-Mental State Examination scores, underscoring their clinical relevance.

These findings demonstrate, for the first time, that nonlinear complexity analyses of resting-state fNIRS can reveal stage-specific neurovascular disruptions across the Alzheimer's spectrum. By identifying robust, interpretable channel-level biomarkers, our framework advances resting-state fNIRS from a supportive technique to a clinically actionable tool for early diagnosis and staging of AD.

1. Introduction

Alzheimer's disease (AD) is a progressive neurodegenerative disorder and the leading cause of dementia in older adults, accounting for 60–70 % of cases worldwide [1]. It is defined by an insidious onset and gradual decline in cognitive domains, particularly memory and executive function, resulting from widespread neuronal loss and cortical atrophy [2]. Pathological processes in AD, including amyloid-β plaque deposition, tau neurofibrillary tangles, and neurovascular dysfunction, begin many years before overt dementia symptoms emerge [3,4]. During this preclinical phase, many individuals present with mild cognitive impairment (MCI), characterized by measurable cognitive deficits that do not meet the criteria for dementia [5]. Early identification of AD and MCI is critical, as it enables timely interventions, supports risk factor management, and allows for implementation of symptom-delaying therapies, all of which can improve patient outcomes and quality of life [6,7].

MCI is recognized as an intermediate state between normal aging and dementia, with approximately 10–15 % of MCI cases progressing to AD each year [8]. Therefore, there is a pressing need for sensitive and specific biomarkers that facilitate the detection of early AD or high-risk MCI, thereby supporting clinical decision-making and long-term care planning [9,10]. Existing diagnostic approaches, including neuropsychological testing and neuroimaging, are limited by modest sensitivity in the early stages of the disease and practical constraints [11,12]. Cognitive screening tools, such as the Mini-Mental State Examination

* Corresponding author at: School of Mechanical Engineering, Pusan National University, 2 Busandaehak-ro, Geumjeong-gu, Busan 46241, South Korea; Institute For Future, School of Automation, Qingdao University, Qingdao 266071, China.
E-mail address: kshong@pusan.ac.kr (K.-S. Hong).

https://doi.org/10.1016/j.bspc.2025.109243
Received 14 July 2025; Received in revised form 21 October 2025; Accepted 16 November 2025
Available online 26 November 2025

(MMSE) and Montreal Cognitive Assessment (MoCA), are widely used but have limited sensitivity for early cognitive decline and can be influenced by educational or cultural background [13]. Neuroimaging modalities such as magnetic resonance imaging (MRI) and positron emission tomography (PET) provide important structural and molecular information but are expensive, non-portable, and not feasible for frequent monitoring [11,14]. Invasive procedures, including lumbar puncture for cerebrospinal fluid analysis, further restrict clinical applicability [15]. These challenges underscore the need for alternative, non-invasive, and cost-effective methods for early detection of AD and MCI [16].

Functional near-infrared spectroscopy (fNIRS) has emerged as a promising non-invasive neuroimaging modality for assessing cortical function [17]. fNIRS operates by measuring changes in oxygenated (*HbO*) and deoxygenated (HbR) hemoglobin concentrations in the cerebral microvasculature, providing real-time insights into regional brain activity [17]. In contrast to MRI and PET, fNIRS is cost-effective, wearable, and does not require specialized facilities [18,19]. The technique allows comfortable placement on the forehead and acquisition of brain signals in outpatient, bedside, or naturalistic settings [14]. fNIRS is well-tolerated in older and vulnerable populations, as it is safe for repeated use, radiation-free, and robust to motion artifacts [20]. These features make fNIRS suitable for large-scale screening of cognitive impairment and longitudinal follow-up [14,21].

Initial fNIRS research in AD and MCI predominantly employed task-based paradigms, demonstrating reduced prefrontal activation during cognitive tasks such as verbal fluency or working memory [22,23]. However, task-based paradigms are constrained by patient cooperation and are susceptible to confounds related to attention, processing speed, and comprehension of instructions [14]. These factors can introduce non-neural variability, complicating the interpretation of neural activation differences. Task-based measures are also influenced by individual motivation and prior experience, limiting standardization and the reliability of repeated assessments. Many patients with advanced cognitive impairment are unable to complete complex tasks, which further limits the clinical utility of task-based fNIRS for large-scale screening or monitoring.

To overcome these limitations, there has been increasing focus on resting-state fNIRS, which measures spontaneous hemodynamic fluctuations with the participant at rest, analogous to resting-state paradigms in fMRI and EEG [14,24,25]. Resting-state fNIRS minimizes task performance confounds, requires little cooperation, and enables the evaluation of intrinsic brain activity [26]. This approach is particularly suitable for elderly or cognitively impaired patients. Recent studies have demonstrated that resting-state fNIRS signals reflect clinically meaningful changes, including altered functional connectivity and alternation in the amplitude and power of low-frequency oscillations in patients with MCI and AD compared to healthy controls [16,27,28,29]. The prefrontal cortex (PFC), which is involved in executive function and memory and is affected early in AD, is particularly accessible to fNIRS and has proven relevant in neurodegeneration research [30].

A central property of resting-state brain activity is its inherent complexity, which reflects the integration of neural populations across multiple spatial and temporal scales [24,31]. In healthy individuals, this complexity is evident as rich, irregular fluctuations in brain signals, which underlie adaptive information processing and functional connectivity [32]. Recent studies have demonstrated that maintaining high complexity and dynamic, time-varying interactions between brain regions is essential for resilience, cognitive flexibility, and efficient information transfer [25,33,34,35]. In contrast, neurodegenerative diseases such as AD are associated with a progressive loss of signal complexity, consistent with the "loss of complexity" hypothesis [35]. As synaptic connectivity and network integrity decline, neural signals become more regular and less adaptive to internal or external challenges [36]. This reduction in complexity has been consistently demonstrated across modalities, including EEG, MEG, and fMRI, using both linear and nonlinear analytic approaches [37,38,39,40].

Entropy-based measures such as spectral entropy (*SE*) and wavelet entropy (*WE*), which quantify the unpredictability and multiscale irregularity of neural signals, have shown significant reductions in AD and MCI patients compared to age-matched controls, often correlating with cognitive impairment and disease progression [41,42]. For example, discrete wavelet transform (DWT)-based *WE* computed from resting EEG is significantly lower in AD and MCI groups than in healthy elders and is strongly correlated with cognitive status [43]. EEG studies also show that lower entropy and reduced fractal dimensionality are associated with more severe cognitive deficits, with Higuchi's fractal dimension (*HFD*) exhibiting lower values in AD patients compared to controls [44,45]. This loss of EEG signal complexity is most pronounced in brain regions vulnerable to AD, such as the parietal cortex, and lower *HFD* values are associated with greater disease severity [45].

Resting-state fMRI and fNIRS studies similarly report reduced spontaneous signal variability in AD [36]; fNIRS work has shown decreased complexity (e.g., multiscale entropy) in AD versus MCI and healthy elders [46], yet higher spectral entropy in the very-low-frequency band (0.008–0.1 Hz) has also been observed in AD, likely reflecting greater vasomotor instability [47]. These observations support a loss-of-complexity framework while revealing domain-specific heterogeneity, underscoring the need to probe complementary domains with metrics that remain robust under short, low-frequency, multi-channel fNIRS recordings, i.e., with low parameter sensitivity, stability with limited data, and clear interpretability. Despite the biomarker relevance of complexity measures across modalities, direct within-dataset comparisons of multiple nonlinear metrics in fNIRS remain rare relative to EEG or fMRI, motivating the present domain-complementary evaluation. Given that resting-state fNIRS typically yields short, low-frequency, multi-channel recordings, metrics with low parameter sensitivity, robustness to limited data length, and clear physiological interpretability are preferable [46]. Time-domain complexity metrics such as multiscale entropy and sample entropy offer scale-wise or short-pattern views but can be length- and parameter-sensitive in resting-state fNIRS, and symbolic measures (permutation entropy) may discard amplitude/spectral detail, limiting hemodynamic interpretability [46,48].

Within this context, we selected *HFD*, *SE*, and *WE* to capture complementary domains of complexity: temporal fractal structure, spectral unpredictability, and time–frequency irregularity. Each of these metrics corresponds to distinct pathophysiological features of AD, including loss of scale-free dynamics, reduced oscillatory organization, and impaired multiscale coordination [41–44]. *HFD* quantifies the temporal fractal structure and overall nonlinearity, reflecting the richness of dynamic neural fluctuations across time [45,49]. *SE* measures the unpredictability and dispersion of spectral power [24,47,50]. *WE* characterizes the distribution of signal energy across time–frequency scales and assess the multiscale irregularity of neural oscillations [39,43,51]. The combined use of these complementary metrics enables comprehensive assessment of both temporal and spectral complexity, which is critical for understanding neurophysiological alterations in AD.

Emerging evidence suggests that neurovascular signal complexity is disrupted across the AD spectrum. Building on this premise, the present study investigates stage-specific alterations in resting-state fNIRS using nonlinear complexity analysis with an emphasis on interpretable, channel-level biomarkers. To our knowledge, few studies have systematically examined multiple complementary complexity metrics within the resting state fNIRS dataset across HC, MCI, and AD. The main contributions of this paper are as follows. (i) To comprehensively evaluate three complementary nonlinear metrics—HFD, SE, and WE—for characterizing neurovascular complexity in HC, MCI, and AD. (ii) To identify stage-sensitive, anatomically localized prefrontal markers through channel-wise and intersection analyses, with particular attention to dorsolateral and frontopolar regions implicated early in AD. (iii) To test mechanistic hypotheses grounded in the loss-of-complexity framework:

namely, that overall temporal complexity decreases with clinical severity (indexed by lower HFD), while entropy-based indices may show metric- and band-dependent deviations reflecting combined neurogenic and vascular influences. (iv) To assess clinical relevance, by examining whether a compact feature set derived from anatomically consistent channels improves group discrimination relative to unconstrained feature sets and by evaluating associations between complexity measures and cognitive status (MMSE). Collectively, these objectives are intended to advance resting-state fNIRS complexity analysis as a scalable, noninvasive, and cognitively undemanding approach that may support early detection and longitudinal monitoring of AD-related neurodegeneration.

Unlike prior fNIRS studies that have primarily focused on binary classification (e.g., AD vs. healthy controls), our work investigates neurovascular complexity across the entire Alzheimer's spectrum, including MCI. By applying nonlinear metrics such as Higuchi's fractal dimension, spectral entropy, and wavelet entropy to resting-state fNIRS signals, we provide a novel framework for capturing subtle stage-specific disruptions. Furthermore, we explore channel-specific biomarkers and validate their anatomical relevance, thereby extending the methodological and clinical utility of resting-state fNIRS in early Alzheimer's detection.

2. Method

2.1. Participants

Participants included 19 patients with Alzheimer's disease (AD; 9 males, 10 females), 37 patients with mild cognitive impairment (MCI; 13 males, 24 females), and 27 healthy controls (HCs; 12 males, 15 females) recruited from Pusan National University Hospital (Busan, Korea). Healthy controls were recruited from the local community, while AD and MCI patients were recruited from the rehabilitation and geriatric departments of Pusan National University Hospital. Individuals with prior neurological or psychiatric disorders, such as schizophrenia, were excluded. The purpose and procedures of the study were fully explained to all participants before enrollment. Written informed consent was obtained from each participant, along with a statement confirming that there was no conflict of interest. After data acquisition, corrupted data sets from four HCs were identified and excluded from further analysis: the final sample comprised 27 HCs (12 males and 15 females).

The Institutional Review Board (IRB) of Pusan National University Hospital approved the study protocol. The diagnosis of MCI was confirmed by a team of psychiatrists and neurosurgeons using several assessments, including the Korean version of the Mini-Mental State Examination (K-MMSE), the Korean-Montreal Cognitive Assessment (K-MoCA), the Seoul Neuropsychological Screening Battery (SNSB), the Clinical Dementia Rating (CDR), and supplementary MRI data. All participants were right-handed, native Korean speakers with similar educational backgrounds. The study adhered to the Declaration of Helsinki [52]. Demographic characteristics, including age, gender, years of education, and K-MMSE scores, for each group are presented in Table 1.

All statistical analyses were conducted using MATLAB R2024a (MathWorks, USA). Statistical significance was defined as $p < 0.05$. A significant age difference was observed between groups ($p < 0.001$). To control for the potential impact of age on cognitive assessment scores, analysis of covariance (ANCOVA) was performed using the MATLAB function aoctool.m, with age included as a covariate. This analysis assessed whether group differences in cognitive performance persisted after adjusting for age. The results indicated that the effect of group (AD vs. MCI vs. HC) on cognitive scores remained significant after controlling for age.

Table 1
Demographic information of participants.

Characteristics	AD (n = 19)	MCI (n = 37)	HC (n = 27)	p-value
Sex (male: female)	9:10	13:24	12:15	0.66
Age (mean ± SD)	77.95 ± 6.56	72.23 ± 6.21	66.46 ± 5.67	<0.01*
Education years (mean ± SD)	9.63 ± 3.60	10.76 ± 3.67	11.14 ± 2.94	0.32
K-MMSE score (mean ± SD)	15.11 ± 1.91	23.84 ± 2.58	28.19 ± 1.44	<0.01*

SD: standard deviation, AD: Alzheimer's disease, MCI: mild cognitive impairment, HC: healthy control, K-MMSE: Korean Version of Mini-Mental State Examination

* indicates p-values with the covariance analysis to compensate for the age difference between groups.

2.2. fNIRS system and data acquisition/preprocessing

In this study, we utilized a portable, wearable continuous-wave fNIRS system (NIRSIT, OBELAB Inc., Korea). The device consisted of 24 near-infrared light sources and 32 detectors, with source-detector distances of approximately 30 mm, yielding up to 204 possible channels. To specifically focus on prefrontal cortex activity and to exclude short-separation channels, a total of 48 channels were selected for analysis. The device was positioned on the forehead, relative to Fpz, according to the international 10–20 system. Channels 1–16 covered the right prefrontal cortex, channels 17–32 the medial prefrontal cortex, and channels 33–48 the left prefrontal cortex. An a priori cap layout map indicating the approximate anatomical locations of each channel (i.e., dorsolateral prefrontal cortex [DLPFC], ventrolateral prefrontal cortex [VLPFC], frontopolar prefrontal cortex [FPFC], and orbitofrontal cortex [OFC]) was constructed and used as a reference for anatomical localization during subsequent visualization of significant channels (see Fig. 1). The system utilized near-infrared light at two wavelengths (780 nm and 850 nm), with a sampling rate of 8.138 Hz. The NIRSIT device was connected via WLAN to a tablet PC for real-time monitoring and data storage.

Data acquisition was conducted in a quiet, dark laboratory environment to minimize external disturbances. Participants were seated comfortably and instructed to remain as still as possible during the resting-state recording session, which lasted approximately 5 min. For consistency, all time-series data were trimmed to 250 s (i.e., 250 s × 8.138 Hz sampling = 2033 data points) per participant for analysis. The signal quality of raw light intensity (780 nm and 850 nm) was inspected for each channel; channels with low signal-to-noise ratios or suspected technical issues were excluded from analysis. Motion artifacts (e.g., abrupt head movements) were detected using a sliding-window motion index (window 0.5-s with ± 0.5-s masking). In addition, channels were discarded if the cumulative excluded duration exceeded 10 % of the 250-s record [53].

During preprocessing, raw intensity changes were converted to concentration changes in *HbO* and *HbR* using the modified Beer-Lambert law. Total hemoglobin (*HbT*) was calculated as the sum of *HbO* and *HbR*. A fourth-order Butterworth band-pass filter (0.0018–0.15 Hz) was applied to *HbO*, *HbR*, and *HbT* signals. The high-pass (0.0018 Hz) removed ultra-slow drift (~0.001 Hz), and the low-pass (0.15 Hz) attenuated respiration (~0.25 Hz) and cardiac (~1 Hz) noise. This band preserved physiologically relevant oscillations, including endothelial (~0.01 Hz), neurogenic (~0.02–0.05 Hz), myogenic (~0.05–0.15 Hz), and Mayer-wave (~0.1 Hz). Noise reduction effectiveness was verified by visual and spectral inspection [54].

2.3. Feature extraction

For each preprocessed channel's 250-second *HbO*, *HbR*, and *HbT*

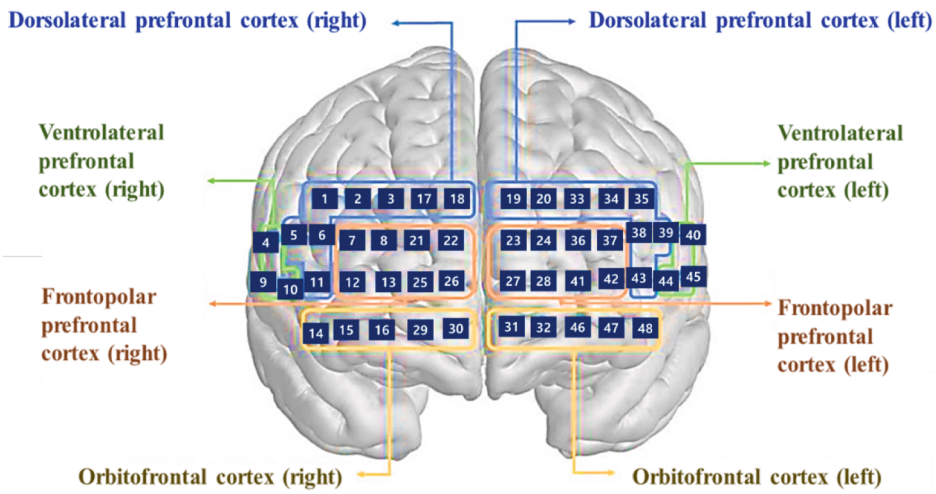

Fig. 1. Optodes configuration of the NIRSIT device (OBELAB, NIRSIT Analysis Tool Manual, 2021).

time series (~2033 data points at 8.138 Hz), three metrics were computed per channel per subject: *HFD*, SE, and *WE*. All implementations were performed in MATLAB. Fig. 2 illustrates representative examples of the feature extraction process, including the log–log plot and regression line for *HFD* estimation, as well as the temporal profiles of *SE* and *WE*.

2.3.1. Higuchi's fractal dimension

HFD quantifies the self-similarity and complexity of a time series, following the method proposed by Higuchi [55,56,57]. For each time series $X = \{x(1), x(2), \ldots, x(N)\}$, a set of new time series is constructed as follows.

$$X_k^m = \left\{ x(m), x(m+k), x(m+2k), \ldots, x\left(m + \left[\frac{N-m}{k}\right]k\right) \right\} \quad (1)$$

where $m = 1, 2, \ldots, k_{\max}$ for each value of k, k-different time series are generated, each starting at a different initial point m. The length of each constructed time series X_k^m is calculated as

$$L_m(k) = \frac{1}{k} \cdot \frac{(N-1)}{\left[\frac{N-m}{k}\right]k} \sum_{i=1}^{\left[\frac{N-m}{k}\right]} |x(m+ik) - x(m+(i-1)k)| \quad (2)$$

For each k, the mean length over all m is computed as

$$L(k) = \frac{1}{k} \sum_{m=1}^{k} L_m(k) \quad (3)$$

A log–log plot of $L(k)$ against $1/k$ is then constructed. The slope of the linear least squares fit of $\log(L(k))$ versus $\log(1/k)$ corresponds to the *HFD* D as follows.

$$\log(L(k)) \propto D \cdot \log(1/k) \quad (4)$$

In this study, the maximum interval length was set to $k_{\max} = 10$, following standard practice [58].

2.3.2. Spectral entropy

SE is a quantitative measure of the complexity or randomness of a signal's power spectrum, based on Shannon's information entropy [50]. For each preprocessed time series $x(t)$, where $t = 0, 1, \ldots, N-1$, *SE* is computed as follows. First, the frequency content of the signal is analyzed by calculating the power spectral density (PSD) via the discrete Fourier transform (DFT) as follows.

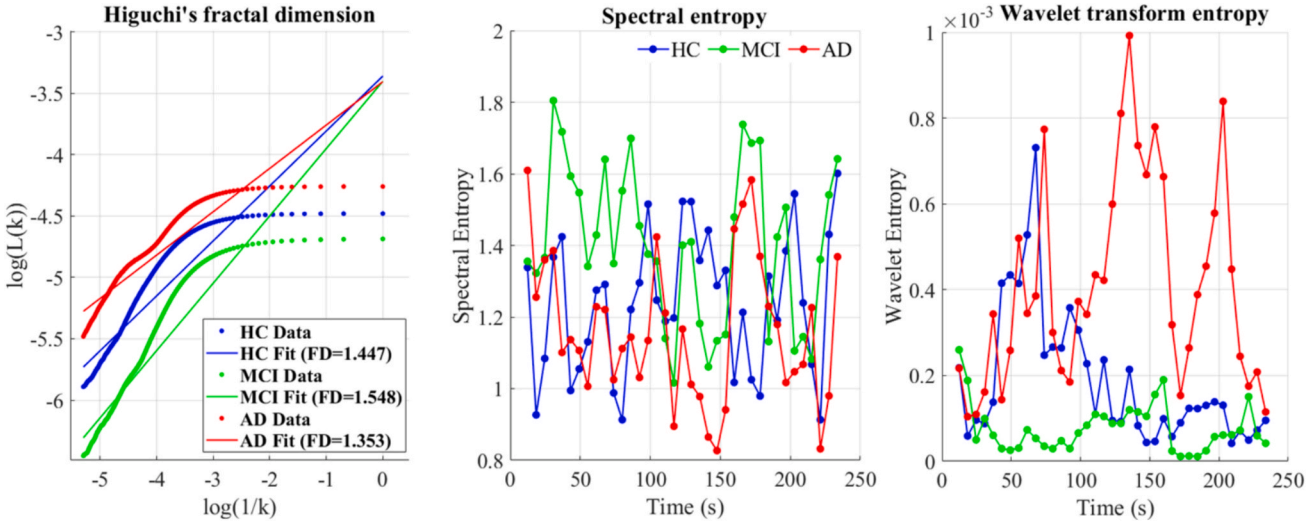

Fig. 2. fNIRS *HbO* signal complexity comparison among HC, MCI, and AD groups. (Left) Log-log plots with linear regression for estimating Higuchi's fractal dimension (*HFD* values labeled), (Middle) spectral entropy profiles, (Right) wavelet transform entropy profiles.

$$X(k) = \sum_{t=0}^{N-1} x(t) \cdot e^{-2\pi ikt/N} \tag{5}$$

where $X(k)$ is the complex Fourier coefficient at frequency index k, and N is the total number of time points. The power spectrum $P(k)$ is then obtained as follows.

$$P(k) = |X(k)|^2 \tag{6}$$

To allow for comparison across signals of different lengths, the power spectrum is normalized:

$$P'(k) = \frac{P(k)}{\sum_k P(k)} \tag{7}$$

where $P'(k)$ represents the relative power at each frequency.

The *SE* is then calculated using the Shannon entropy formula applied to the normalized power distribution as follows.

$$SE = -\sum_{k=1}^{n} P'(k) \cdot \log P'(k) \tag{8}$$

where n is the total number of frequency bins. For normalization and comparability across different conditions, *SE* is divided by the theoretical maximum entropy, $\log n$, yielding a normalized *SE* value bounded between 0 and 1 [59]:

$$SE_{norm} = \frac{SE}{\log n} \tag{9}$$

A higher value of normalized *SE* indicates a more uniform (random) power distribution across frequencies, reflecting greater signal complexity, while a lower value indicates concentration of power in fewer frequency bands, reflecting greater regularity or predictability.

2.3.3. Wavelet entropy

WE is a nonparametric measure that quantifies the degree of order or disorder in multi-frequency brain signals, capturing the uncertainty in the energy distribution across different time–frequency scales derived from the DWT [60]. Each signal is decomposed using the DWT with a selected mother wavelet (i.e., Daubechies-4) into $v_0 + 1$ resolution levels [61]. For a given analysis window i, the DWT produces a set of coefficients $C_{i,j}(k)$ at each resolution level $j (j = 0, 1, \ldots, v_0)$ and time index k.

The total energy in window i was computed as follows.

$$E_{i,tot} = \sum_{j=0}^{v_0} \sum_{k} \left| C_{i,j}(k) \right|^2 \tag{10}$$

The energy at each level j was calculated as follows.

$$E_{i,j} = \sum_{k} \left| C_{i,j}(k) \right|^2 \tag{11}$$

The normalized (relative) energy at each resolution level is defined as

$$p_{i,j} = \frac{E_{i,j}}{E_{i,tot}} \tag{12}$$

The set $\{p_{i,j}\}$ forms a probability distribution of energy across the wavelet scales. *WE* is then computed as the Shannon entropy of the relative energy distribution:

$$WE_i = -\sum_{j=0}^{v_0} p_{i,j} \log p_{i,j} \tag{13}$$

For comparability across different numbers of wavelet levels, *WE* is normalized by dividing by the maximum possible entropy, $\log(v_0 + 1)$ as follows.

$$WE_{i,norm} = \frac{WE_i}{\log(v_0 + 1)} \tag{14}$$

A higher *WE* indicates a more uniform (i.e., more disordered) distribution of energy across the wavelet scales, whereas a lower *WE* reflects concentration of signal energy in fewer bands, implying greater order or regularity.

Each metric (*HFD*, *SE*, *WE*) has been computed separately for *HbO*, *HbR*, and *HbT*, yielding a matrix of [numChannels × 1] per metric for each subject. These matrices are stored for subsequent statistical analyses. All computations are based on the same filtered, artifact-corrected signals and applied consistent parameter settings across all subjects and channels. For machine learning analyses, metric values are standardized within training folds; for reporting group-level results, raw metric values or *z*-scores (as specified) are used. All parameter settings and code are version-controlled and documented to ensure full reproducibility.

2.4. Statistical analysis

All statistical analyses were performed using MATLAB R2024a (MathWorks, USA). A two-tailed *p*-value of less than 0.05 was considered statistically significant. To assess the distribution of each complexity metric—*HFD*, *SE*, and *WE*—the Shapiro–Wilk test [62] was applied across subjects and channels. As the majority of distributions deviated from normality, nonparametric statistical methods were primarily employed.

1) Global (across-channel) group-level comparisons

For each chromophore (*HbO*, *HbR*, *HbT*) and each complexity metric, the mean feature value across all 48 channels was computed per subject. Group differences among AD, MCI, and HC were assessed using the Kruskal–Wallis test [5]. When a significant effect was detected ($p < 0.05$), Dunn-Sidak corrections were applied to control the familywise error rate (FWER) [63]. For each pairwise comparison, corrected *p*-values, effect sizes (e.g., rank-biserial correlation), and 95 % confidence intervals were reported.

2) Channel-wise analysis and multiple comparisons correction

To investigate localized effects, channel-wise Kruskal–Wallis tests were conducted for each metric–chromophore combination (i.e., 3 chromophores × 3 metrics × 48 channels). For channels demonstrating significant group differences, pairwise comparisons were performed using the Dunn-Sidak correction. For significant channels, group-wise descriptive statistics (mean ± SD) and corresponding *p*-values were reported.

3) Intersection Analysis of Significant Channels

To identify channels showing convergent alterations across complexity metrics, an intersection analysis was performed. For each chromophore, the list of channels meeting Dunn–Sidak corrected significance ($p < 0.05$) for *HFD*, *SE*, and *WE* was compiled. Pairwise intersections (*HFD* ∩ *WE*, *HFD* ∩ *SE*, *WE* ∩ *SE*) and the three-way intersection (*HFD* ∩ *SE* ∩ *WE*) were extracted and tabulated. For each intersecting channel, corrected *p*-values, effect sizes, and group-wise statistics were documented. Channels consistently exhibiting significant changes across multiple metrics were designated as core candidate biomarkers, providing insight into the spatial patterns and potential diagnostic relevance of the observed effects.

2.5. Classification and ROC analysis

To assess the diagnostic utility of fNIRS-derived complexity metrics,

we implemented supervised multiclass classification and receiver operating characteristic (ROC) analysis. For feature representation, we considered two sets: (i) a full-channel set, where HFD, SE, and WE were extracted from all 48 channels for each chromophore (HbO, HbR, HbT), and (ii) a compact, biologically informed core-channel set, in which a subset of "core" channels was selected based on the intersection of channels showing statistically significant group differences across multiple features and chromophores, as determined by channel-wise group comparisons (see Section 2.4). The set of core channels was predetermined from an independent analysis and kept fixed across all cross-validation folds to avoid information leakage. For each subject, the values of HFD, SE, and WE from these core channels were concatenated across chromophores to construct a multimodal feature vector.

To benchmark the state-of-the-art approaches, we trained ten classifiers: bagged decision tree (BDT), linear discriminant analysis (LDA), logistic regression (LR), support vector machine (SVM), k-nearest neighbor (KNN), random forest (RF), extreme gradient boosting (XGBoost), gradient boosting decision tree (GBDT), random undersampling boosting (RUSBoost), and artificial neural network (ANN) [64,65,66]. For the 10-way model benchmarking, we used the core-channel feature set (ii) exclusively. After identifying the single best-performing classifier based on cross-validated AUC on the core-channel set, we then compared feature sets (i) vs. (ii) only for that best classifier, using DeLong's test for correlated ROC curves to assess whether the biologically informed reduction preserved or improved discriminative performance [67].

All features were processed within each training fold to prevent data leakage. z-score standardization was applied using the mean and standard deviation computed from the training set and then applied to the corresponding test fold; for tree-based models, features were used in their original scale. We employed repeated stratified 5-fold cross-validation ($k = 5$, repeats $= 10$) to maintain a balanced representation of AD, MCI, and HC and to obtain stable out-of-sample estimates. During model training, class weights were set inversely proportional to group frequencies. Implementation details and hyperparameter settings for all models are summarized in Supplementary Table 1. All analyses were conduted in MATLAB.

We used a one-vs-all ROC framework and computed per-class AUCs from classifier probabilities. For each model, AUCs were averaged across folds and the 10 repeats and reported as mean ± SD and 95 % confidence intervals (95 % CI). The 95 % CI was obtained via nonparametric bootstrap (1,000 iterations) with subject-level resampling of pooled held-out predictions. For formal feature-set comparison, DeLong's test for correlated ROC curves was applied only to the best-performing classifier (selected by cross-validated AUC) to compare core-channel vs. full-channel models. DeLong's test is a nonparametric procedure that leverages the relative rankings of positives vs. negatives to estimate each model's AUC variance and the covariance between AUCs under paired predictions on the same subjects, yielding a z-statistic whose p-value quantifies the significance of the AUC difference.

2.6. Correlation with MMSE scores

To assess the association between cognitive function and complexity metrics, we calculated correlations between Mini-Mental State Examination (MMSE) scores and channel-specific features. Due to the non-normal distribution of the data, Spearman's rank correlation was primarily employed. To additionally evaluate linear associations and for comparison, Pearson's correlation was also computed when the data met the assumptions of normality. This dual approach allowed the assessment of both monotonic and linear relationships, enhancing the robustness and interpretability of the findings.

To adjust for potential confounding effects of age, sex, and education, partial correlations were computed using residuals: both the complexity metric and MMSE score were regressed on the covariates, and the correlation between the resulting residuals was calculated. For each analysis, we reported the correlation coefficient (Pearson's r and Spearman's ρ), p-value, and 95 % confidence intervals estimated via bootstrap resampling (1,000 iterations). Scatter plots were generated with MMSE scores on the x-axis and complexity metric values on the y-axis, color-coded by diagnostic group (AD, MCI, HC), with regression lines included for visualization.

3. Results

3.1. Group differences in fNIRS-based features across AD progression

To investigate the differences in hemodynamic signal complexity among the AD, MCI, and HC groups, we extracted three features—*HFD*, *SE*, and *WE*—from *HbO*, *HbR*, and *HbT* signals across all 48 channels. For each participant, feature values were computed for every channel and then averaged across channels to obtain subject-level means. Group-level mean and standard deviation values were subsequently calculated, and statistical comparisons were performed using the Kruskal-Wallis test, followed by post hoc Dunn–Sidak corrections for pairwise group comparisons. All indices demonstrated statistically significant group-level differences ($p < 0.05$), indicating altered signal characteristics across the AD continuum.

For *HbO* signals, *HFD* showed a clear increasing trend from AD (1.8411 ± 0.1101) to MCI (1.9013 ± 0.0942) and HC (1.9117 ± 0.0751), with statistically significant differences between AD and MCI ($p < 0.0001$) as well as between AD and HC ($p < 0.0001$). However, the difference between MCI and HC was not significant ($p = 0.5849$). *SE* showed a non-monotonic pattern with a slight dip in the MCI group and was significant only between AD vs. MCI ($p = 0.0020$) and AD vs. HC ($p = 0.0018$) but not between MCI vs. HC ($p = 0.9909$). *WE* values were highest in AD and comparably lower in MCI and HC, with significant differences only between AD and the other two groups.

In *HbR* signals, the *HFD* again showed a consistent ascending trend (AD: 1.9090 ± 0.0874 < MCI: 1.9475 ± 0.0652 < HC: 1.9583 ± 0.0536), with all comparisons significant ($p < 0.0001$); see Fig. 3. *SE* followed a similar trend to *HbO*, with AD showing significantly higher values than MCI and HC, while MCI and HC did not differ ($p = 0.7535$). Notably, *SE* values were highest in the AD group, decreased slightly in the MCI group, and showed a slight rebound in the HC group, reflecting a non-monotonic pattern across disease stages. WE values decreased from AD to HC, but no significant difference was found between MCI and HC ($p = 0.9985$), further confirming that this index may be more sensitive in distinguishing AD from other groups.

For *HbT*, *HFD* again exhibited a gradual increase across the disease spectrum, with significant group differences between AD vs. MCI and AD vs. HC ($p < 0.0001$), but not between MCI vs. HC ($p = 0.7506$). *SE* and *WE* followed similar patterns as observed in *HbR* and *HbO*. Specifically, both *SE* and *WE* were highest in the AD group, showed a slight reduction in MCI, and then slightly increased again in the HC group. Among them, *WE* showed the only significant difference between MCI vs. HC ($p = 0.0373$), while *SE* did not reach significance for that comparison ($p = 0.5040$); see Table 2.

3.2. Channel-wise statistical analysis of fNIRS entropy metrics

Building on the group-level trends reported in Section 3.1, we further interrogated every feature × chromophore × channel combination across the complete 48-channel prefrontal montage. Channels reaching $p < 0.05$ in the Kruskal–Wallis test were retained for post hoc Dunn–Sidak contrasts and classified as "robust" when at least two pairwise contrasts were significant or as "single-contrast" when only one contrast survived. The absolute number of significant channels is summarized in Table 3, and detailed statistical results for all key channels are provided in Supplementary Table 2.

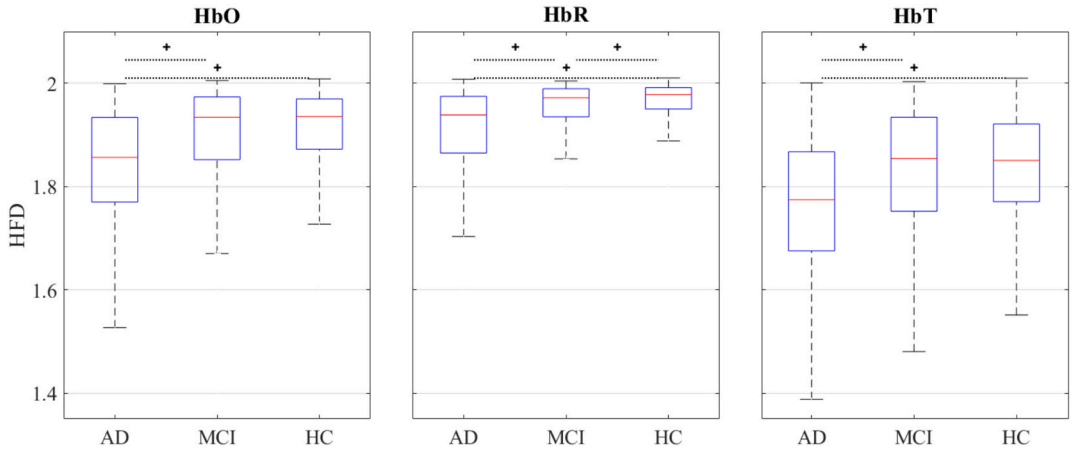

Fig. 3. Distribution of *HFD* values across groups and hemoglobin signals. Statistical significance of pairwise comparisons is indicated (+indicates $p < 0.05$).

Table 2
Group-wise comparison of fNIRS-derived features across AD, MCI, and HC. Values are presented as mean ± standard deviation. Kruskal-Wallis and pairwise comparisons were used to assess statistical differences. (SD: standard deviation).

Hemodynamic signal	Complexity Metric	AD (Mean ± SD)	MCI (Mean ± SD)	HC (Mean ± SD)	Kruskal-Wallis *p*	Post-hoc: Dunn-Sidak		
						AD vs MCI	AD vs HC	MCI vs HC
HbO	**HFD**	1.8411 ± 0.1101	1.9013 ± 0.0942	1.9117 ± 0.0751	$p < 0.0001$	$p < 0.0001$	$p < 0.0001$	0.5849
	SE	0.8030 ± 0.0755	0.7911 ± 0.1094	0.8024 ± 0.0575	0.0007	0.0020	0.0018	0.9909
	WE	0.0917 ± 0.0721	0.0699 ± 0.0683	0.0705 ± 0.0668	$p < 0.0001$	$p < 0.0001$	$p < 0.0001$	0.5849
HbR	**HFD**	1.9090 ± 0.0874	1.9475 ± 0.0652	1.9583 ± 0.0536	$p < 0.0001$	$p < 0.0001$	$p < 0.0001$	$p < 0.0001$
	SE	0.7972 ± 0.0738	0.7868 ± 0.1091	0.7978 ± 0.0583	$p < 0.0001$	$p < 0.0001$	$p < 0.0001$	0.7535
	WE	0.0761 ± 0.0740	0.0603 ± 0.0666	0.0596 ± 0.0656	$p < 0.0001$	$p < 0.0001$	$p < 0.0001$	0.9984
HbT	**HFD**	1.7653 ± 0.1303	1.8337 ± 0.1227	1.8355 ± 0.1033	$p < 0.0001$	$p < 0.0001$	$p < 0.0001$	0.7506
	SE	0.8003 ± 0.0744	0.7880 ± 0.1084	0.7986 ± 0.0558	$p < 0.0001$	$p < 0.0001$	$p < 0.0001$	0.5039
	WE	0.1022 ± 0.0763	0.0779 ± 0.0715	0.0789 ± 0.0647	$p < 0.0001$	$p < 0.0001$	$p < 0.0001$	0.0372

Table 3
Summary of significant channels per complexity metric.

Complexity metric	HbO	HbR	HbT	Total features (% of montage)
HFD	31 (17 R + 14 S)	31 (12 R + 19 S)	20 (9 R + 11 S)	**82 / 144 tests**
SE	4 (2 R + 2 S)	6 (1 R + 5 S)	2 (2 R + 0 S)	**12 / 144 tests**
WE	5 (1 R + 4 S)	4 (3 R + 1 S)	5 (0 R + 5 S)	**14 / 144 tests**

R = robust channel (≥2 contrasts); S = single-contrast channel.

3.2.1. *Global extent of channel-wise significance*

Across the 432 tested combinations (3 entropy metrics × 3 hemodynamic parameters × 48 channels), 108 (25 %) demonstrated significant effects. As the disease progressed from HC to AD, loss of fractal complexity (*HFD*↓) was the predominant finding, accounting for 82 significant channels (31 *HbO*, 31 *HbR*, 20 *HbT*). In comparison, *SE* increases (*SE*↑) were relatively focal (12 channels), and *WE* increases (*WE*↑) occupied an intermediate position (14 channels). Robust effects—those showing significance for both AD vs. MCI and AD vs. HC—were observed in 47 channels, whereas 61 channels exhibited significance in only a single contrast. The spatial distribution of significant channels is illustrated in the brain maps shown in Fig. 4.

3.2.2. *Channel-wise alterations in Higuchi fractal dimension*

For *HbO*, robust reductions in *HFD* (i.e., significant for both AD vs. MCI and AD vs. HC) were observed bilaterally, with a pronounced emphasis in the left-hemisphere. In the right-hemisphere, channels 3 and 17 (right DLPFC) and channels 8, 21, 22, and 26 (right FPFC) demonstrated AD < MCI and AD < HC. In the left-hemisphere, robust loci were concentrated in the frontopolar and dorsolateral regions: channels 24, 28, 36, 37, and 41 (left FPFC) and channels 34, 38, and 43 (left DLPFC). Additional robust sites included channel 30 (right OFC) and channels 47 and 48 (left OFC), demonstrating progressive fractal-complexity loss in the bilateral executive-control regions, with greater involvement in the left-hemisphere.

With *HbR*, robust reductions in *HFD* separated AD from both MCI and HC across multiple frontal loci. In the right-hemisphere, channel 3 (right DLPFC) and channels 8, 12, 22, 25, and 26 (right FPFC) showed AD < MCI and AD < HC. On the left, channel 20 (left DLPFC) and channels 24, 27, 36, and 41 (left FPFC) also exhibited robust significance. Notably, channel 31 (left OFC) differentiated both AD and MCI from HC (HC < MCI ≈ AD), indicating a marker of general pathology rather than a specific disease stage. The remaining robust *HbR* channels consistently reflected a progressive loss of fractal complexity with increasing disease severity.

Regarding *HbT*, robust *HFD* decreases (AD < MCI & AD < HC) were detected at channels 3 and 8 (right DLPFC/FPFC), and in the left-hemisphere at channels 20, 24, 33, 34, and 38 (left DLPFC), as well as channels 36 and 37 (left FPFC). These left-dominant patterns indicate the dorsolateral and frontopolar regions as primary locations for hemodynamic complexity reduction in AD.

Beyond these robust multi-contrast sites, for *HbR*, channel 9 (right VLPFC) significantly distinguished MCI from HC, but not MCI from AD, indicating fractal-complexity changes occurring prior to clinical AD diagnosis. Single-contrast channels—where significance was observed

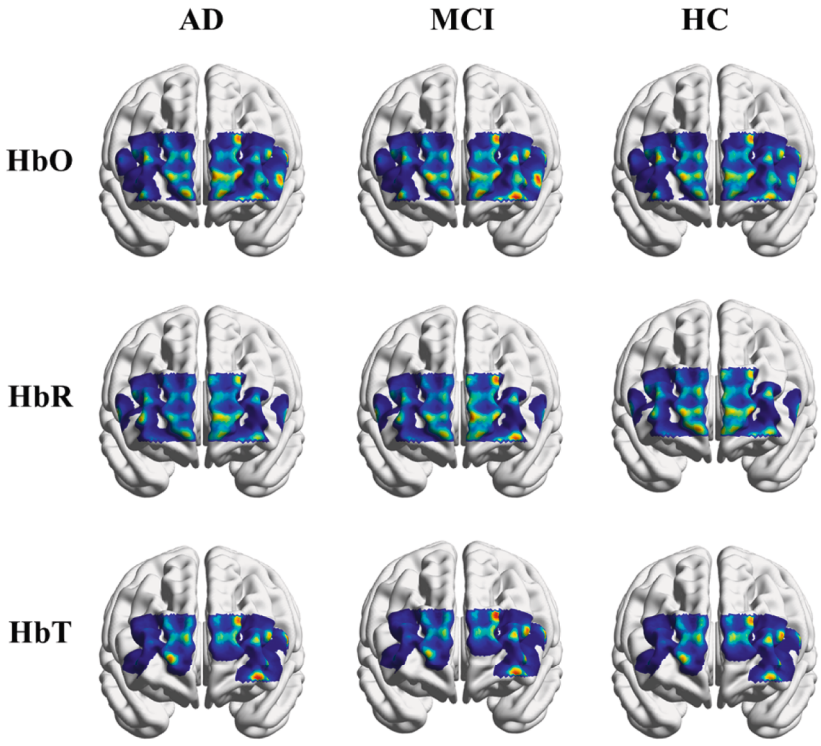

(a) *HFD*

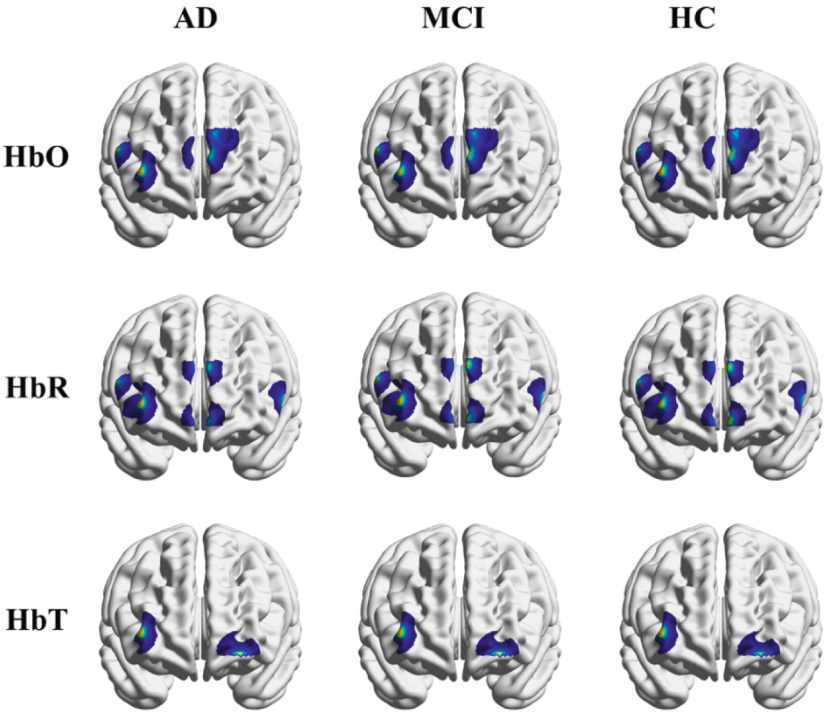

(b) *SE*

Fig. 4. Brain maps showing the spatial distribution of significant channels for group comparisons ($p < 0.05$): (a) Higuchi's Fractal Dimension (*HFD*), (b) Spectral Entropy (*SE*), and (c) Wavelet Entropy (*WE*).

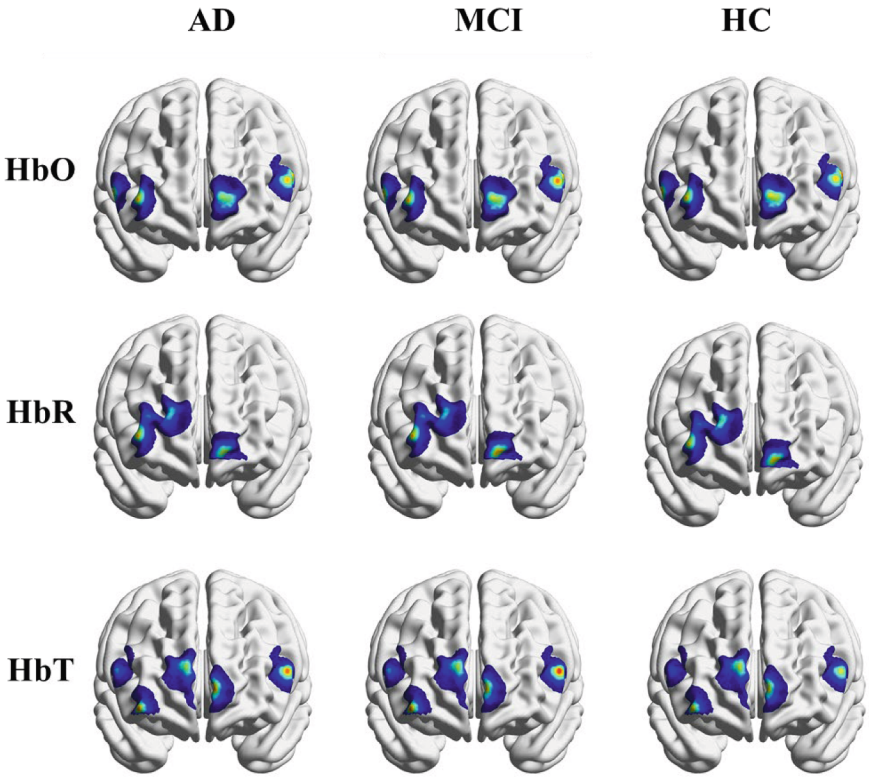

(c) *WE*

Fig. 4. (*continued*).

only between AD vs. HC or AD vs. MCI—were distributed across DLPFC, VLPFC, FPFC, and OFC regions, representing potential exploratory markers.

In summary, fractal-complexity loss was widely observed across the prefrontal cortex, with a notable left-hemisphere dominance for *HbO* and *HbT*, and bilateral frontopolar/dorsolateral involvement for *HbR*. Most robust channels differentiated AD from both MCI and HC, highlighting their value for stage-specific differentiation. A smaller subset, such as *HbR* channel 31, differentiated both patient groups (MCI and AD) from HC without stage specificity, while *HbR* channel 9 specifically differentiated prodromal MCI from HC.

3.2.3. Channel-wise alterations in spectral entropy

For *HbO*, channels 12 (right FPFC) and 23 (left FPFC) showed higher *SE* in AD than in MCI and HC, indicating progressive spectral flattening in bilateral frontopolar regions. For *HbR*, channel 11 (right DLPFC) likewise exhibited higher *SE* in AD versus MCI and HC. For *HbT*, channel 12 also showed elevated *SE* in AD, demonstrating channel-12 consistency across chromophores; channel 46 (left OFC) showed higher *SE* in both patient groups than in HC (HC $<$ MCI $\approx$ AD), suggesting general cognitive impairment.

Exploratory single-contrast *SE* elevations appeared mainly in the right VLPFC (e.g., *HbO* channel 4 and *HbR* channel 4) and in the left DLPFC (*HbT* channel 20). Overall, robust *SE* increases localized to frontopolar cortex (*HbO* channels 12 and 23 and *HbT* channel 12) and right DLPFC (*HbR* channel 11), whereas left OFC (*HbT* channel 46) indexed broader pathology.

3.2.4. Channel-wise alterations in wavelet entropy

For *HbO*, channel 12 (right FPFC) exhibited robust *WE* increases in AD compared with MCI and HC, consistent with its *SE* findings. In the case of *HbR*, channels 8 and 12 (right FPFC) and 32 (left OFC) demonstrated significant *WE* increases in AD compared to MCI and HC. Regarding *HbT*, no channels showed robust *WE* increases; significant *WE* elevations in total hemoglobin were limited to single-contrast findings (e.g., channels 5, 15, 22, 27, 39), indicating these as exploratory. All anatomically defined metric patterns are summarized in Table 4.

3.3. Intersection analysis and biomarker hierarchy

3.3.1. Intersection analysis

To synthesize the channel- and metric-specific findings into a coherent panel of candidate biomarkers, we identified channels exhibiting robust alterations in *HFD*, *SE*, or *WE* (defined as significant differences for both AD vs. MCI and AD vs. HC) across one or more hemodynamic signals; see Table 5.

– Triple-intersection hotspot: Channel 12 (right FPFC).

Channel 12 showed robustness across *HFD*, *SE*, and *WE* and across multiple chromophores: *HFD* decreased in *HbR* (AD $<$ MCI and AD $<$ HC), *SE* increased in *HbO* and *HbT*, and *WE* increased in *HbO* (AD $>$ MCI and AD $>$ HC across the stated contrasts). Thus, channel 12 integrates *HbR* complexity loss with *HbO/HbT* entropy elevation and serves as a multimodal AD biomarker in the right FPFC.

– Dual-intersection: *HFD* and *WE* at channel 8 (right FPFC).

Channel 8 showed *HFD* decreases in *HbO/HbR/HbT* (AD $<$ MCI and AD $<$ HC) and a *WE* increase in *HbR* (AD $>$ MCI and AD $>$ HC), capturing both reduced complexity and heightened irregularity in the right FPFC.

Table 4
Robust (two pairwise contrasts were significant) channel locations and cortical sub-regions for each complexity metric.

Complexity Metric	Hemodynamic signal	Channel No.	Anatomical Location	Comparison
HFD↓	HbO	24, 28, 36, 37, 41	Left FPFC Left DLPFC	AD < MCI, AD < HC
		34, 38, 43 47, 48	Left OFC	
		3, 17	Right DLPFC	AD < MCI,
		8, 21, 22, 26	Right FPFC Right OFC	AD < HC
		30		
	HbR	3	Right DLPFC	AD < MCI,
		8, 12, 22, 25, 26	Right FPFC Left DLPFC	AD < HC MCI < HC,
		20	Left FPFC	AD < HC
		24, 27, 36, 41	Left OFC	
		31		
	HbT	3	Right DLPFC,	AD < MCI,
		8	Right FPFC	AD < HC
		20, 24, 33, 34, 38	Left DLPFC Left FPFC	
		36, 37		
SE↑	HbO	12	Right FPFC	AD > MCI,
		23	Left FPFC	AD > HC
	HbR	11	Right DLPFC	AD > MCI, AD > HC
	HbT	12	Right FPFC,	AD > MCI,
		46	Left OFC	AD > HC; MCI > HC, AD > HC
WE↑	HbO	12	Right FPFC	AD > MCI, AD > HC
	HbR	8, 12	Right FPFC,	AD > MCI,
		32	Left OFC	AD > HC
	HbT	–	–	–

Table 5
Intersection-based prefrontal channels with convergent nonlinear complexity metric changes for staging Alzheimer's disease.

Channel	Region	Hemodynamic signal	Complexity Metrics	Pattern
12	Right FPFC	HbO(SE,WE), HbR (HFD), HbT(SE)	HFD, SE, WE	AD versus MCI & AD versus HC
8	Right FPFC	HbO(HFD), HbR(HFD, WE), HbT(HFD)	HFD, WE	
3	Right DLPFC	HbO, HbR, HbT	HFD	
24	Left FPFC			
36	Left FPFC			
22	Right FPFC	HbO, HbR		
26	Right FPFC			
41	Left FPFC			
34	Left DLPFC	HbO, HbT		
37	Left FPFC			
38	Left DLPFC			
20	Left DLPFC	HbR, HbT		

– Channels with robust multi-hemodynamic intersection in *HFD*.

Multi-chromophore *HFD* reductions were observed at *HbO/HbR/HbT* channel 3 (right DLPFC), 24 (left FPFC), 36 (left FPFC); *HbO/HbR* channel 22, 26 (right FPFC), 41 (left FPFC); *HbO/HbT* channel 38, 34 (left DLPFC), 37 (left FPFC); *HbR/HbT* channel 20 (left DLPFC). Collectively, these locations implicate bilateral prefrontal regions, particularly the dorsolateral and frontopolar cortices, as consistent sites of reduced complexity across AD progression.

3.3.2. *Stage-specific biomarkers*

Several additional channels, such as *HbR* channel 9 (for MCI vs. HC), *HbR* channel 31 (for HC vs. patients), and *HbT* channel 46 (for HC vs. patients), exhibited significant differences only for a single feature-chromophore combination, without overlap across other metrics or modalities. Although these channels were not included in the robust multi-metric intersections, they were identified as exploratory biomarkers for MCI detection or broader cognitive pathology. Based on the intersection analysis and anatomical localization, we delineated three main biomarker panels.

First, a prodromal MCI screening panel was defined, as channel 9 in the right VLPFC significantly differentiated MCI from HC, reflecting fractal complexity loss that emerges at the MCI stage before AD.

Second, a broad pathology screening panel included channels that distinguished both patient groups (MCI and AD) from HC, specifically *HbR* channel 31 (left OFC, *HFD*) and *HbT* channel 46 (left OFC, *SE*), which may be useful for detecting general pathology relative to healthy controls.

Third, for high-specificity AD confirmation, we highlight right FPFC channels 12 and 8: channel 12 showed *HFD* alterations in *HbR* with *SE* increases in *HbO/HbT* and *WE* increases in *HbO*, while channel 8 showed *HFD* reductions in *HbO/HbR/HbT* with *WE* increases in *HbR*. Additional multi-chromophore *HFD* alterations were observed across dorsolateral/frontopolar regions (channels 3, 24, 36, 22, 26, 41) and the left DLPFC/FPFC (channels 34, 37, 38, 20). Together, these loci distinguished AD from both MCI and HC when combining fractal, spectral, and wavelet metrics across HbO, HbR, and HbT signals.

Overall, these biomarker panels are anchored to anatomically

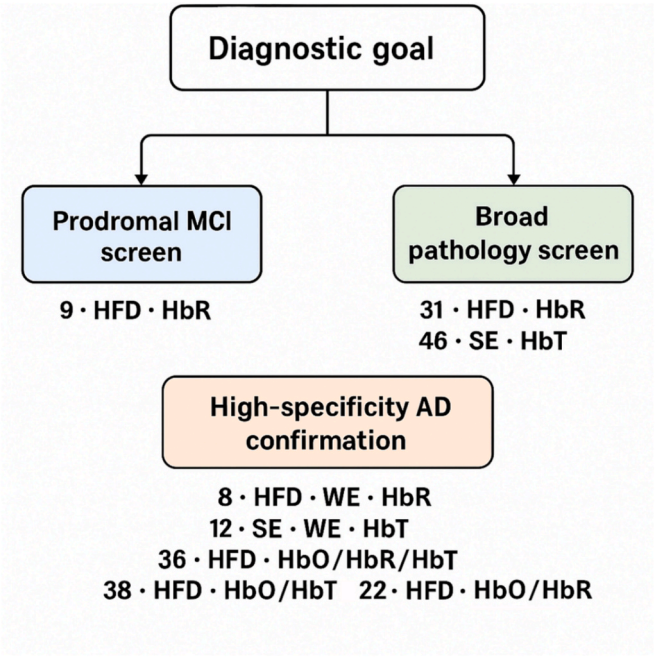

Fig. 5. Schematic flow of stage-specific biomarker panels for fNIRS-based dementia screening and confirmation.

distinct cortical regions—right ventrolateral for prodromal MCI screening, left orbitofrontal for broad pathology detection, and bilateral frontopolar/dorsolateral regions for AD confirmation—thus underscoring both the sensitivity for early detection and the specificity for AD diagnosis; see Fig. 5.

3.4. Classification performance

Building on the group-level findings (Sections 3.1–3.3), we benchmarked ten supervised classifiers on the core-channel feature set—BDT, LDA, LR, SVM, KNN, RF, XGBoost, GBDT, RUSBoost, and ANN. Performance was estimated with repeated stratified 5-fold cross-validation (100 repeats), using a one-vs-all ROC framework. For each model, AUCs were averaged across folds and repeats and summarized as mean ± SD with 95 % confidence intervals computed by nonparametric subject-level bootstrap (1,000 iterations).

From the model-comparison results on the core-channel feature set, the bagged decision tree (BDT) achieved the highest AUC (0.876, 95 % CI [0.871, 0.880]), followed by ANN (0.839, [0.812, 0.862]), RF (0.835, [0.827, 0.843]), LR (0.832, [0.821, 0.844]), and LDA (0.832, [0.806, 0.861]). SVM (0.821, [0.814, 0.831]), GBDT (0.794, [0.775, 0.812]), KNN (0.780, [0.768, 0.790]), RUSBoost (0.779, [0.766, 0.803]), and XGBoost (0.764, [0.751, 0.790]) showed comparatively lower performance. Fig. 6 summarizes these benchmarks (a) and presents the AD one-vs-all ROC curves (b), consistent with the ranking.

Following Methods (Section 2.5), we therefore used the best-performing classifier (BDT) to conduct the formal core-channel vs. full-channel comparison. The core-channel multimodal BDT yielded AUCs of 0.889 (AD vs. non-AD), 0.728 (MCI vs. non-MCI), and 0.686 (HC vs. non-HC) in Fig. 7, with corresponding operating metrics summarized in Table 6 (accuracy: 0.867/0.795/0.781; sensitivity: 0.842/0.730/0.654; specificity: 0.893/0.835/0.852; F1-score: 0.854/0.751/0.742; all values mean ± SD across repeated stratified 5-fold CV). By contrast, full-channel models produced consistently lower AUCs. For example, using HFD features, full-channel HbO achieved 0.805 (AD), 0.518 (MCI), and 0.557 (HC); HbR achieved 0.746, 0.498, and 0.658; and HbT achieved 0.670, 0.630, and 0.562 for AD/MCI/HC, respectively. SE and WE on full-channel inputs were weaker still, with AD AUCs barely reaching the 0.6 range. These patterns are summarized visually in Fig. 8, in which the core-channel bars (purple) exceed all full-channel counterparts across classes and chromophores.

To assess statistical significance on paired predictions from the same subjects, we applied DeLong's test for correlated ROC curves only to the BDT (per Methods). Core-channel models showed significant gains over full-channel models for HFD–HbO (AD: $p = 0.015$; MCI: $p < 0.0001$; HC: $p < 0.0001$) and HFD–HbR (AD: $p < 0.0001$; MCI: $p < 0.0001$; HC: $p = 0.2473$, n.s.), and for HFD–HbT (AD: $p < 0.0001$; MCI: $p < 0.0001$; HC: $p = 0.003$). Collectively, these results confirm that intersection-derived core channels provide significantly better discriminability, with the largest relative improvements observed for MCI.

3.5. Correlation between MMSE scores and fNIRS-derived features

To examine the cognitive relevance of extracted nonlinear complexity features, Pearson's and Spearman's correlation coefficients between each feature and MMSE scores across all subjects were calculated. Only features with statistically significant correlations ($p < 0.05$) and correlation coefficients within a predefined moderate-to-strong range ($|r|$ or $|\rho| \geq 0.3$) were selected for analysis. All selected features met this criterion in both correlation types. Among these, the top-ranking features by correlation strength for each metric are presented in Table 7.

Notably, a total of 50 *HFD*-based features (aggregated across *HbO*, *HbR*, and *HbT*), 6 *SE*-based features, and 9 *WE*-based features showed statistically significant and directionally consistent correlations with MMSE scores. While these associations do not confirm direct causality, they indicate a potential relationship between signal complexity measures and cognitive performance.

Here, r represents Pearson's correlation coefficient, and ρ represents Spearman's correlation coefficient. Among the most robust correlations, *HFD* in *HbO* and *HbR* signals at prefrontal locations were prominent, particularly channels 22, 26, and 36 in the right and left FPFC, demonstrating strong positive correlations (e.g., *HFD HbO* channel 22: $r = 0.5093$, $\rho = 0.4652$; *HFD HbR* channel 22: $r = 0.5046$, $\rho = 0.4658$). These results align with earlier findings (Sections 3.2-3.3), where significant *HFD* reductions at these channels differentiated AD from MCI and HC groups. The correlations indicate these channels' sensitivity to general cognitive decline and suggest that higher hemodynamic complexity is associated with higher cognitive function. In addition to frontopolar regions, DLPFC locations, such as channel 38 (*HFD HbO*: $r =$

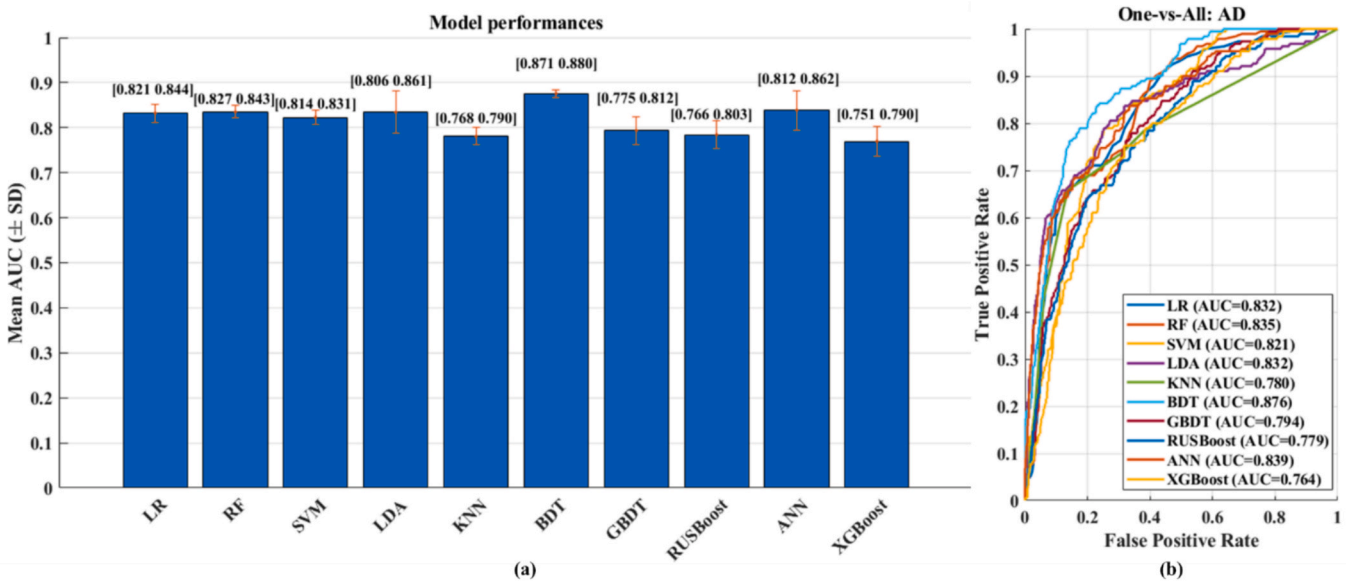

Fig. 6. Benchmarking of ten classifiers on the core-channel feature set with class-wise ROC (AD). (a) Mean AUC (±SD) for ten classifiers evaluated with repeated stratified 5-fold CV (100 repeats) on the core-channel feature set. 95 % CIs (in brackets above bars) were obtained via nonparametric subject-level bootstrap (1,000 iterations) from pooled held-out predictions. (b) One-vs-all ROC curves for AD vs. non-AD on the same core-channel setup.

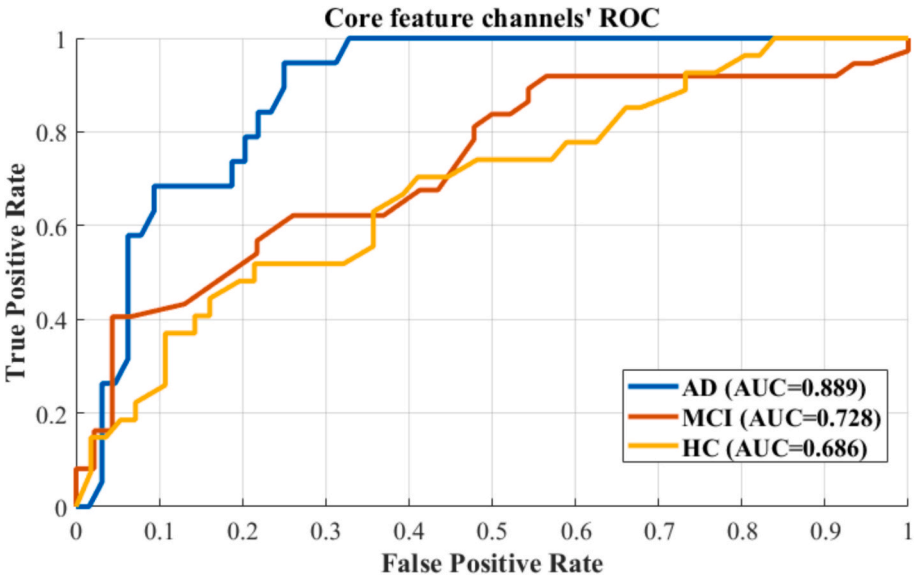

Fig. 7. ROC curves for the classification of AD, MCI, and HC using features extracted from intersection-derived core channels (*HbO*, *HbR*, *HbT*).

Table 6
Five-fold cross-validation performance metrics for AD, MCI, and HC using features extracted from intersection-derived core channels (mean ± standard deviation).

Performance Metric	AD vs non-AD	MCI vs non-MCI	HC vs non-HC
AUC	0.889 ± 0.021	0.728 ± 0.038	0.686 ± 0.045
Accuracy	0.867 ± 0.033	0.795 ± 0.027	0.781 ± 0.035
Sensitivity (Recall)	0.842 ± 0.041	0.730 ± 0.051	0.654 ± 0.059
Specificity	0.893 ± 0.036	0.835 ± 0.044	0.852 ± 0.041
F1-Score	0.854 ± 0.038	0.751 ± 0.053	0.742 ± 0.055

0.4696, $\rho = 0.4109$) also showed significant correlations.

SE and *WE* measures also demonstrated significant negative correlations with MMSE scores, especially in the right prefrontal channels. For example, *SE HbR* channel 12 showed a strong negative correlation (r = -0.3526, ρ = -0.3948). Similarly, *WE HbT* channel 5 exhibited a negative correlation (r = -0.3399, ρ = -0.4342), indicating increased multiscale irregularity associated with lower cognitive scores.

These findings establish a coherent biomarker framework combining group-level contrasts, intersection analysis, and MMSE correlations for diagnostic and cognitive monitoring purposes. For visual reference, top-ranked features with the strongest correlations are illustrated in Fig. 9, highlighting the relationship between nonlinear complexity metrics and MMSE scores across different hemodynamic signals.

4. Discussion and future work

This study systematically examined how fNIRS-based nonlinear complexity metrics (*HFD*, *SE*, and *WE*) of hemodynamic signals change across the AD spectrum and identified the prefrontal cortical regions that exhibit the most prominent changes. The key findings were that, as AD progresses, the fractal complexity of cortical hemodynamic signals markedly decreases while signal irregularity (as reflected by entropy measures) significantly increases, especially in the AD group. Notably, *HFD* values decreased progressively from HC and MCI to AD, while *SE* and *WE* values were higher (indicating increased randomness) in AD than in earlier stages. There were also differences in sensitivity among the metrics and chromophores: *HFD* most robustly distinguished AD from MCI and HC, although its discrimination between MCI and HC was relatively lower. *SE* and *WE* showed stepwise group differences mainly in certain signals (*HbO*, *HbR*, or *HbT*), indicating that each chromophore and each metric has a different sensitivity to the disease stage.

These results suggest that as AD pathology advances, neural network activity becomes less complex and more random, consistent with the known neurodegenerative processes of synaptic loss and network disintegration in AD [68,69]. Reduced signal complexity implies a decline in the brain's adaptive capacity, which is characteristic of AD's neuropathology [69]. Conversely, increases in entropy measures reflect more irregular and desynchronized neural activity, aligning with theories of cortical "randomization" due to synaptic and neuronal loss in AD. Notably, synaptic loss is the strongest anatomical correlate of cognitive decline in AD [68], and this loss of connectivity directly contributes to reduced complexity and organization of brain signals. Our findings reinforce the pathophysiological link between AD-related structural degeneration (synapse/neuron loss) and functional signal alterations (lower complexity, higher randomness).

These nonlinear complexity metrics could improve the sensitivity and specificity of AD detection. The apparent differences observed, especially between AD and non-AD groups, suggest that these metrics provide diagnostic information that complements conventional measures. Similar patterns of reduced complexity and increased irregularity have been consistently reported in other modalities, such as EEG and fMRI in AD [47,70]. For instance, resting-state fMRI analyses have shown that the multiscale entropy of BOLD signals is highest in healthy controls and progressively declines through MCI to AD [70], and EEG studies have demonstrated that AD patients' brain signals exhibit lower fractal dimensions and a shift toward more random frequency content compared to healthy controls [36]. In a recent fNIRS study focusing on *SE*, AD patients had significantly higher entropy in resting-state hemoglobin signals than controls [47], indicating a loss of dominant oscillatory rhythms. These convergent findings support the idea that complexity metrics decrease and irregularity metrics increase in AD, strengthening their validity as robust biomarkers of the AD process [36,69]. Notably, our study demonstrates these changes using a resting-state, noninvasive fNIRS paradigm with high discrimination power, underscoring the clinical utility of fNIRS-based nonlinear complexity analysis for AD.

Regionally, alterations were most consistent in the dorsolateral and frontopolar prefrontal cortices. The DLPFC—central to executive control—shows reduced functional connectivity, metabolism, and synaptic integrity in AD/MCI [71,72]; concordantly, our data indicate decreased *HFD* (with entropy increases) in DLPFC, most prominently on the left (hotspot channels, e.g., 34/38; right-hemisphere analogs similar). The

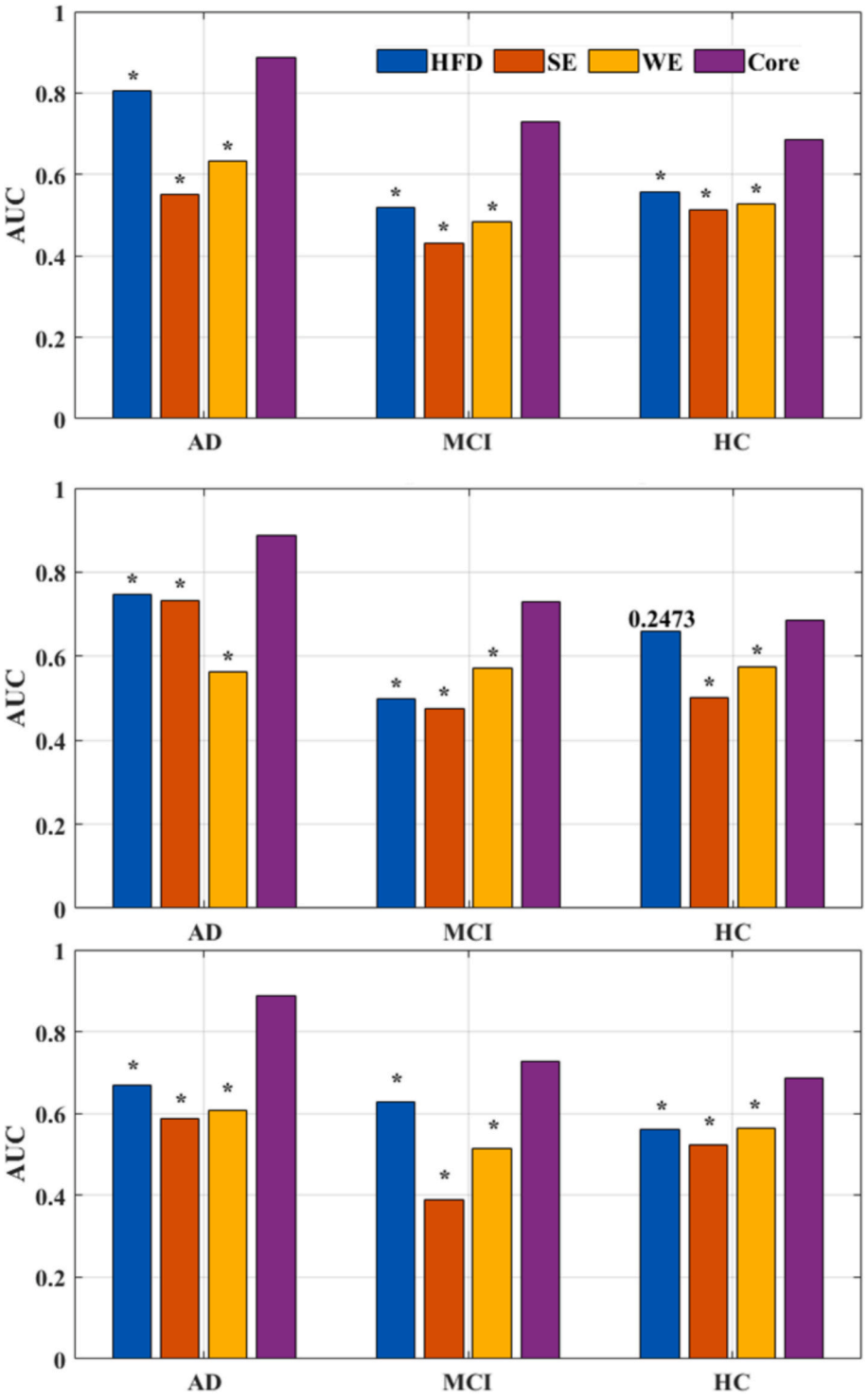

Fig. 8. AUC comparison for AD, MCI, and HC classification across three hemodynamic signals (*HbO*, *HbR*, *HbT*). * denote statistically significant improvements in core-channel versus full-channel AUC by paired DeLong's test ($p < 0.05$).

frontopolar cortex (BA10) likewise exhibited marked abnormalities (e.g., channels 8/12), identifying FPFC/DLPFC as convergent "hotspots" where multiple metricfs change together. Secondary but less consistent effects appeared in orbitofrontal and ventrolateral regions—OFC (e.g., 31/32) tied to affective–reward processes and linked to apathy/disinhibition in AD [73], and VLPFC (e.g., 9) showing early alterations, particularly in MCI.

This topography suggests hemisphere- and region-specific vulnerability: our left-predominant FPFC/DLPFC complexity loss aligns with reports of early left frontal involvement, tau accumulation, and connectivity/metabolic decline in dorsal/frontopolar prefrontal areas, as well as frontal atrophy preceding clinical dementia [71,72]. Practically, these "hotspot" channels motivate a compact, prefrontal-targeted montage for screening and monitoring; isolated early-stage changes outside the core set may serve as exploratory predictors of conversion. Consistent with their roles in higher-order cognition, FPFC/DLPFC alterations also tracked cognitive status in our cohort.

Our intersection analysis, overlapping results across multiple metrics

Table 7
Correlation of fNIRS features with MMSE.

Metric	Signal	Channel	Region	Pearson's *r*	*p*-value	Spearman's *ρ*	*p*-value	Direction
HFD	HbO	22	right FPFC	0.5093	< 0.0001	0.4652	< 0.0001	↑ with MMSE
HFD	HbR	22	right FPFC	0.5046	< 0.0001	0.4658	< 0.0001	↑ with MMSE
HFD	HbO	36	left FPFC	0.5036	< 0.0001	0.4212	< 0.0001	↑ with MMSE
HFD	HbO	38	left DLPFC	0.4696	< 0.0001	0.4109	< 0.0001	↑ with MMSE
HFD	HbO	21	left FPFC	0.4026	< 0.0001	0.4035	< 0.0001	↑ with MMSE
SE	HbR	12	right FPFC	−0.3526	0.0011	−0.3948	< 0.0001	↓ with MMSE
SE	HbT	12	right FPFC	−0.3253	0.0027	−0.3488	0.0012	↓ with MMSE
WE	HbT	5	right OFC	−0.3399	0.002	−0.4342	< 0.0001	↓ with MMSE
WE	HbR	32	Left OFC	−0.3197	0.0032	−0.3837	0.0003	↓ with MMSE

FPFC = frontopolar prefrontal cortex, DLPFC = dorsolateral prefrontal cortex, OFC = orbitofrontal cortex. Arrows indicate direction of association.

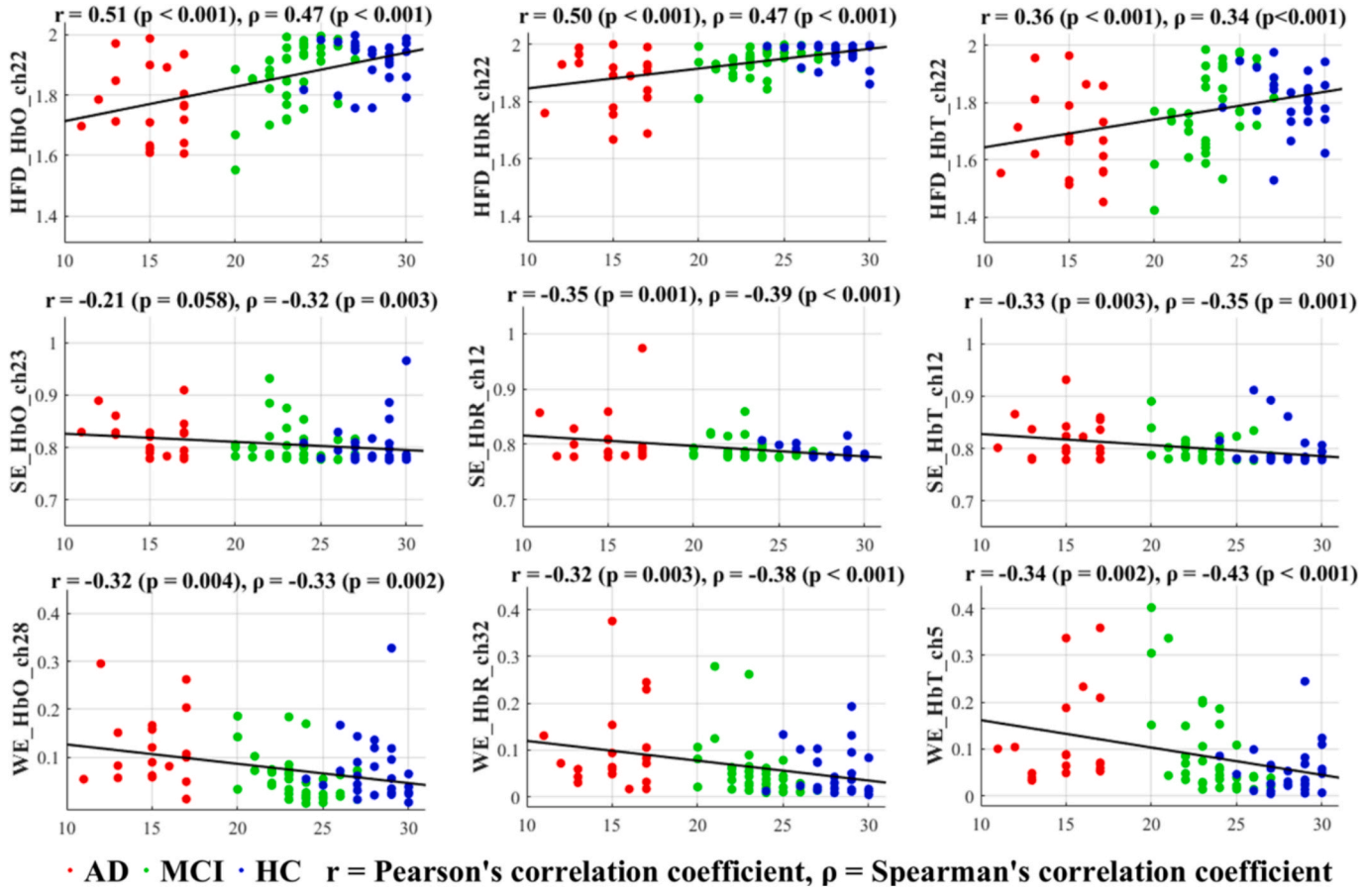

Fig. 9. Top-ranked correlations between nonlinear complexity metrics and MMSE scores for each hemodynamic signal.

and signals, provided further insight into robust biomarkers. Certain channels, such as channel 12 in our montage (right frontopolar cortex, AAL3 brain atlas: #6 Right middle frontal gyrus), showed consistent and significant changes in *HFD*, *SE*, and *WE* simultaneously, indicating multi-metric convergence unlikely to reflect false positives. These convergent channels formed stage-specific panels that suggest an ordered progression of cortical involvement and offer compact, noise-resistant inputs for machine-learning models. Anatomically, the AAL3 designates the right middle frontal gyrus (MFG) as region #6, a core node of the executive-control (frontoparietal) network subserving working memory, attention, and executive functions [74]. The right MFG is thus a plausible early-detection indicator in prodromal AD and MCI: task-based fMRI consistently shows hypoactivation [74], while at rest, early AD exhibits disrupted intrinsic connectivity that includes the right MFG [75,76], and MCI patients tend to co-activate the DMN with right frontal regions when the DMN is engaged [77,78]. These domains are affected early in AD, and the supporting networks (including DLPFC/MFG) show functional compromise; taken together, convergent atlas-based and functional evidence indicate that the right MFG (AAL6) participates deeply in the networks degraded in early AD, with patients across the prodromal stage showing hypoactivation, connectivity loss, and compensatory changes [74,78].

Recent fNIRS–machine-learning studies (2023–2025) report a wide range of performance depending on paradigm and modality. In resting-state, fNIRS-only Alzheimer's disease studies, reported AUCs are typically around ~ 0.70 (e.g., 0.708) [65], whereas approaches incorporating neuropsychological tests or task-based paradigms have achieved substantially higher discrimination (up to ~ 0.97) [65,79]. In stroke, resting-state feature models reached AUC = 0.715, while task-evoked fNIRS improved to AUC = 0.861 [66].

To ensure methodological consistency and comparability, we followed recent fNIRS–ML practices and benchmarked ten commonly used

model families (informed by [65,66]). In our results, the BDT model achieved the highest macro AUC on the core-channel features (0.876; 95 % CI [0.871, 0.880], estimated via subject-level bootstrap with 1,000 iterations), followed by ANN, RF, LR, and LDA, with SVM, GBDT, KNN, RUSBoost, and XGBoost performing lower. Resting-state hemodynamics represent inherently complex and nonlinear neurovascular processes that cannot be fully captured by linear transformations. Accordingly, ensemble models such as BDT can improve prediction accuracy and stability by employing bootstrapping to reduce variance, while also providing a flexible framework for risk classification and capturing nonlinear dependencies in complex data structures without prior interaction specification [64]. Several models, particularly ANN, RF, LR, and LDA, also showed promising performance. This pattern likely reflects those nonlinear methods (ANN, RF) can model complex inter-feature relationships in hemodynamic signals, whereas linear models (LR, LDA) remain effective when discriminative information is concentrated in a few dominant core channels. Taken together, these findings indicate that both nonlinear and linear approaches are promising for classifying complexity-based features in resting-state fNIRS data.

Despite cross-study differences in cohorts and pipelines, our core-channel, complexity-based approach within a resting-state fNIRS–only framework yielded higher cross-validated discrimination in our cohort (AD AUC = 0.889). Using the best-performing model (BDT), we conducted the prespecified core- vs. full-channel comparison: the core-channel multimodal classifier achieved AUCs of 0.889 (AD), 0.728 (MCI), and 0.686 (HC) with consistent operating metrics (Table 6), whereas full-channel variants were lower across chromophores and feature families. Paired DeLong tests indicated significant gains for core channels in most settings (Fig. 8), with the most pronounced relative improvements for MCI. In our cohort, biologically informed channel selection improved discriminability relative to naïve full-channel inputs.

Consistent with the broader literature, task-based and multimodal designs often report higher accuracy by adding informative variance beyond resting hemodynamics—e.g., schizophrenia vs. MDD under verbal fluency (up to 0.998) [80], ADHD multimodal fusion (AUC = 0.892) [81], depression with robust feature engineering (AUC = 0.919–0.935) [82,83], and Huntington's disease multimodal work (AUC = 0.963) [84]. Against this backdrop, our resting-only framework—integrating core-channel selection with nonlinear complexity metrics—achieved AUC = 0.889 for multiclass AD staging, highlighting the diagnostic discrimination achievable from purely resting-state fNIRS features when appropriately modeled.

Collectively, these examples and recent model-selection guidelines [76,79] suggest that while resting-state paradigms effectively capture intrinsic neurovascular dynamics, they often yield lower discriminative performance compared with task-evoked or multimodal approaches. In contrast, our resting-only framework—integrating core-channel selection with nonlinear complexity metrics—achieved a robust AUC of 0.889 in multiclass AD staging, highlighting the diagnostic potential of purely resting-state fNIRS features when appropriately modeled.

We also explored correlations between fNIRS metrics and standard clinical cognition scores (e.g., MMSE). Notably, *HFD* showed a positive correlation with MMSE (i.e., higher complexity was associated with better cognitive scores), whereas *SE* and *WE* showed negative correlations. These correlations were especially robust in the key channels identified earlier. This convergence between biomarker channels and those showing cognitive correlations reinforces the clinical validity of the fNIRS metrics. Thus, fNIRS nonlinear complexity measures could be used to track cognitive decline or improvement within a patient over time, offering a quantitative tool for disease progression or treatment response. This, combined with the portability of fNIRS and its suitability for real-time, repeated measurements, makes it well-suited for both clinical and community use.

In summary, we observe reduced complexity (*HFD*↓) and elevated entropy (*SE*/*WE*↑) in the prefrontal cortex—most prominently in DLPFC/FPFC/OFC—consistent with prior multimodal patterns in AD [66,70]. Convergent evidence across EEG, fMRI, MEG, and fNIRS reinforces these metrics as core disease features [80]. Methodologically, we add intersection-based biomarker mapping and a task-free, spatially resolved approach that moves fNIRS beyond supportive monitoring toward clinically interpretable staging.

This study contributes several innovations to the field. First, we demonstrate the value of resting-state fNIRS for stage-specific characterization across AD, MCI, and HC groups, an area that has been underexplored compared to task-evoked paradigms. Second, by prioritizing nonlinear complexity metrics and validating a robust biomarker channel with anatomical mapping, we highlight novel avenues for clinically interpretable neurovascular markers. Finally, our machine learning framework, which incorporated cross-validation stability and classifier comparisons, provides methodological robustness within the present cohort and scope.

Taken together, the findings are promising; however, this is a preliminary study with a modest sample, and larger longitudinal cohorts are needed to confirm robustness and generalizability and to track intra-individual change, including MCI → AD conversion. External validation across multiple cohorts was not feasible for practical and structural reasons specific to resting-state AD fNIRS research: (i) to the best of our knowledge, no publicly available resting-state AD fNIRS repositories currently exist; (ii) device and protocol heterogeneity (source–detector geometry, wavelengths, cap density, resting duration, eyes-open/closed, preprocessing pipelines) would require harmonization and site-effect correction prior to pooling; (iii) privacy/IRB and data-use limitations constrain cross-site sharing of clinical neuroimaging data in memory-disordered populations; (iv) class imbalance and phenotypic heterogeneity (e.g., comorbidities, medications) complicate matched aggregation; and (v) high intra-individual variability in resting signals suggests that personalized baselines or longitudinal calibration may be needed before robust cross-site generalization. We therefore frame the present findings as a single-cohort proof of concept and highlight multi-center harmonization and data sharing as explicit goals for future work.

Beyond cohort expansion, multimodal fusion—combining fNIRS complexity features with EEG, fMRI, or structural MRI—should cross-validate biomarkers and improve early-stage sensitivity and specificity. Given the observed MMSE associations, developing wearable or bedside tools for real-time monitoring and adaptive feedback would enable personalized tracking. Extending the framework to vascular dementia, Parkinson's disease, and frontotemporal dementia may reveal disease-specific signatures and broaden clinical utility. Finally, clinical deployment will require optimizing low-density cap designs, real-time algorithms, and noise-robust feature extraction across diverse populations and settings. Given the noninvasiveness and portability of fNIRS, nonlinear complexity analysis remains a promising tool for brain health monitoring and early intervention in AD.

5. Conclusion

In conclusion, resting-state fNIRS-derived complexity (*HFD*) and entropy (*SE*, *WE*) metrics reliably differentiate Alzheimer's disease (AD), mild cognitive impairment (MCI), and healthy controls (HC), revealing distinct patterns of neural complexity reduction and signal irregularity increase with progression of AD. Notably, *HFD* demonstrated the highest discriminatory power, with the greatest number of statistically significant channels distinguishing patient groups, suggesting it is the most sensitive indicator among the three metrics. Particularly pronounced decreases in fractal complexity were observed in the bilateral frontopolar and dorsolateral prefrontal cortex, highlighting these regions as early targets of AD pathology. Intersection analysis identified robust biomarker channels, notably channel 12 in the right frontopolar cortex, consistently affected across multiple nonlinear complexity measures. Machine learning analyses demonstrated that models built upon these core channels significantly outperform models using all channels, indicating that targeted fNIRS measurements could enhance diagnostic

accuracy. Additionally, strong correlations between fNIRS metrics and cognitive assessments underscore their clinical relevance. These findings support the development of fNIRS-based nonlinear complexity metrics as practical, non-invasive tools for early AD diagnosis, staging, and longitudinal cognitive monitoring, potentially improving clinical management and outcomes for individuals with neurodegenerative conditions.

CRediT authorship contribution statement

Min-Kyoung Kang: Writing – original draft, Validation, Software, Methodology, Formal analysis, Data curation. **Keum-Shik Hong:** Writing – review & editing, Supervision, Project administration, Funding acquisition, Conceptualization. **Yong-Il Shin:** Resources, Methodology, Conceptualization. **Guanghao Huang:** Writing – review & editing, Validation.

Ethics approval and consent to participate

All experiments were approved by the Institutional Review Board (IRB) of Pusan National University Yangsan Hospital and conducted per institutional guidelines for ethical procedures and scientific management (IRB Approval No: PNUYH-03–2018-003). We obtained informed consent from all the participants or their guardians.

Declaration of competing interest

The authors declare that they have no known competing financial interests or personal relationships that could have appeared to influence the work reported in this paper.

Acknowledgment

This work was supported by the National Research Foundation of Korea funded by the Ministry of Science and ICT, Korea (grant no. IRIS-2023-00207954).

Appendix A. Supplementary material

Supplementary data to this article can be found online at https://doi.org/10.1016/j.bspc.2025.109243.

Data availability

Data will be made available on request.

The data are not publicly available due to privacy or ethical restrictions.

References

[1] P. Kamatham, R. Shukla, D. Khatri, L. Vora, Pathogenesis, diagnostics, and therapeutics for Alzheimer's disease: breaking the memory barrier, Ageing Res. Rev. 101 (2024) 102481, https://doi.org/10.1016/j.arr.2024.102481.
[2] M. DeTure, D. Dickson, The neuropathological diagnosis of Alzheimer's disease, Mol. Neurodegener. 14 (2019) 32, https://doi.org/10.1186/s13024-019-0333-5.
[3] A. Serrano-Pozo, M. Frosch, E. Masliah, B. Hyman, Neuropathological alterations in Alzheimer disease, Cold Spring Harb. Perspect. Med. 1 (2011) a006189, https://doi.org/10.1101/cshperspect.a006189.
[4] S.-H. Yoo, S.-W. Woo, M.J. Shin, J.A. Yoon, Y.I. Shin, K.-S. Hong, Diagnosis of mild cognitive impairment using cognitive tasks: a functional near-infrared spectroscopy study, Curr. Alzheimer Res. 17 (2020) 1145–1160, https://doi.org/10.2174/1567205017666201125093735.
[5] Y. Shou, L. Gao, Z. Zhang, J. Han, J. Dai, H. Pan, Z. Zhao, Y. Weng, C. Chen, J. Wang, Disentangling normal and pathological brain atrophy for the diagnosis of mild cognitive impairment and Alzheimer's disease, Biomed. Signal Process. Control 100 (2025) 106955, https://doi.org/10.1016/j.bspc.2024.106955.
[6] S. Cheng, P. Shang, Y. Zhang, J. Guan, Y. Chen, Z. Lv, S. Huang, Y. Liu, H. Xie, An fNIRS representation and fNIRS-scales multimodal fusion method for auxiliary diagnosis of amnestic mild cognitive impairment, Biomed. Signal Process. Control 96 (2024) 106646, https://doi.org/10.1016/j.bspc.2024.106646.
[7] P. Rosenberg, C. Lyketsos, Mild cognitive impairment: searching for the prodrome of Alzheimer's disease, World Psychiatry 7 (2008) 72–78, https://doi.org/10.1002/j.2051-5545.2008.tb00173.x.
[8] A. Eschen, M. Martin, U. Gasser, M. Kliegel, Prospective and retrospective memory complaints in mild cognitive impairment and mild Alzheimer's disease, Brain Impairment 10 (2009) 59–75, https://doi.org/10.1375/brim.10.1.59.
[9] V.P. Subramanyam Rallabandi, K. Seetharaman, Classification of cognitively normal controls, mild cognitive impairment and Alzheimer's disease using transfer learning approach, Biomed. Signal Process. Control 79 (2023) 104092, https://doi.org/10.1016/j.bspc.2022.104092.
[10] A. Porsteinsson, R. Isaacson, S. Knox, M. Sabbagh, I. Rubino, Diagnosis of early Alzheimer's disease: Clinical practice in 2021, J. Prev Alzheimers Dis. 8 (2021) 371–386. https://doi.org/10.14283/jpad.2021.23.
[11] C. Dang, Y. Wang, Q. Li, Y. Lu, Neuroimaging modalities in the detection of Alzheimer's disease-associated biomarkers, Psychoradiology 3 (2023) kkad009, https://doi.org/10.1093/psyrad/kkad009.
[12] N. Naseer, K.-S. Hong, FNIRS-based brain-computer interfaces: a review, Front. Hum. Neurosci. 9 (2015) 3, https://doi.org/10.3389/fnhum.2015.00003.
[13] O. Pedraza, J.H. Clark, S.E. O'Bryant, G.E. Smith, R.J. Ivnik, N.R. Graff-Radford, F. B. Willis, R.C. Petersen, J.A. Lucas, Diagnostic validity of age and education corrections for the Mini-Mental State Examination in older African Americans, J. Am. Geriatr. Soc. 60 (2012) 328–331, https://doi.org/10.1111/j.1532-5415.2011.03766.x.
[14] D. Yang, Y.I. Shin, K.-S. Hong, Systemic review on transcranial electrical stimulation parameters and EEG/fNIRS features for brain diseases, Front. Hum. Neurosci. 15 (2021) 629323, https://doi.org/10.3389/fnhum.2021.629323.
[15] E. Giannella, V. Notarangelo, C. Motta, G. Sancesario, Biobanking for neurodegenerative diseases: challenge for translational research and data privacy, Neuroscientist 29 (2023) 190–201, https://doi.org/10.1177/10738584211036693.
[16] K.-S. Hong, A. Zafar, Existence of initial dip for BCI: an illusion or reality, Front. Neurorobotics 12 (2018) 69, https://doi.org/10.3389/fnbot.2018.00069.
[17] N. Wang, et al., Functional near-infrared spectroscopy for the assessment and treatment of patients with disorders of consciousness, Front. Neurol. 16 (2025) 1524806, https://doi.org/10.3389/fneur.2025.1524806.
[18] S. Hosni, S. Borgheai, J. McLinden, Y. Shahriari, An fNIRS-based motor imagery BCI for ALS: a subject-specific data-driven approach, IEEE Trans. Neural Syst. Rehabil. Eng. 28 (2020) 3063–3073, https://doi.org/10.1109/TNSRE.2020.3038792.
[19] D. Yang, M.-K. Kang, G. Huang, A.T. Eggebrecht, K.-S. Hong, Repetitive Transcranial Alternating Current Stimulation to Improve Working memory: an EEG-fNIRS Study, IEEE Trans. Neural Syst. Rehabil. Eng. 32 (2024) 1257–1266, https://doi.org/10.1109/TNSRE.2024.3384283.
[20] B. Edlow, J. Claassen, N. Schiff, D. Greer, Recovery from disorders of consciousness: mechanisms, prognosis and emerging therapies, Nat. Rev. Neurol. 17 (2021) 135–156, https://doi.org/10.1038/s41582-020-00427-7.
[21] M. Buegler, et al., Digital biomarker-based individualized prognosis for people at risk of dementia, Alzheimers Dement. Diagn. Assess. Dis. Monit. 12 (2020) e12073, https://doi.org/10.1002/dad2.12073.
[22] C. Duan, Y. Chong, J. Gong, Q. Wu, J. Sun, C. Zheng, Z. Li, L. Xia, Z. Cheng, P. Zhang, W. Xia, An fNIRS-based investigation of cerebral hemodynamic responses during verbal fluency task and n-back task in individuals with mild cognitive impairment, Front. Neurol. 16 (2025) 1571964, https://doi.org/10.3389/fneur.2025.1571964.
[23] M.-K. Kang, K.-S. Hong, D. Yang, H.K. Kim, Multi-scale neural networks classification of mild cognitive impairment using functional near-infrared spectroscopy, Biocybernetics Biomed. Eng. 45 (2025) 11–22, https://doi.org/10.1016/j.bbe.2024.12.005.
[24] L. Wang, T. Du, L. Zhao, Y. Shi, W. Zeng, Research on the lateralization of brain functional complexity in mild cognitive impairment-Alzheimer's disease progression based on multiscale lateralized brain entropy, Biomed. Signal Process. Control 86 (2023) 105216, https://doi.org/10.1016/j.bspc.2023.105216.
[25] C. Chang, G.H. Glover, Time–frequency dynamics of resting-state brain connectivity measured with fMRI, Neuroimage 50 (2010) 81–98, https://doi.org/10.1016/j.neuroimage.2009.12.011.
[26] J. Wang, Q. Dong, H. Niu, The minimum resting-state fNIRS imaging duration for accurate and stable mapping of brain connectivity network in children, Sci. Rep. 7 (2017) 6461, https://doi.org/10.1038/s41598-017-06340-7.
[27] R.S. Huang, K.-S. Hong, Multi-channel-based differential pathlength factor estimation for continuous-wave fNIRS, IEEE Access 9 (2021) 37386–37396, https://doi.org/10.1109/ACCESS.2021.3062861.
[28] H. Niu, J. Wang, T. Zhao, N. Shu, Y. He, Revealing topological organization of human brain functional networks with resting-state functional near infrared spectroscopy, PLoS One 7 (2012) e45771, https://doi.org/10.1371/journal.pone.0045771.
[29] A. Zafar, K.-S. Hong, Detection and classification of three-class initial dips from prefrontal cortex, Biomed. Opt. Express 8 (2017) 367–383, https://doi.org/10.1364/BOE.8.000367.
[30] N. Friedman, T. Robbins, The role of prefrontal cortex in cognitive control and executive function, Neuropsychopharmacology 47 (2022) 72–89, https://doi.org/10.1038/s41386-021-01132-0.
[31] E. Hansen, D. Battaglia, A. Spiegler, G. Deco, V. Jirsa, Functional connectivity dynamics: modeling the switching behavior of the resting state, Neuroimage 105 (2015) 525–535, https://doi.org/10.1016/j.neuroimage.2014.11.001.
[32] D. Garrett, G. Samanez-Larkin, S. MacDonald, U. Lindenberger, A. McIntosh, C. Grady, Moment-to-moment brain signal variability: a next frontier in human

brain mapping? Neurosci. Biobehav. Rev. 37 (2013) 610–624, https://doi.org/10.1016/j.neubiorev.2013.02.015.
[33] R.M. Hutchison, T.W. Womelsdorf, E.A. Allen, P.A. Bandettini, V.D. Calhoun, M. Corbetta, P.S. Della, J.H. Duyn, G.H. Glover, J. Gonzalez-Castillo, D. A. Handwerker, S. Keilholz, V. Kiviniemi, D. Leopold, F. de Pasquale, O. Sporns, M. Walter, C. Chang, Dynamic functional connectivity: promise, issues, and interpretations, Neuroimage 80 (2013) 360–378, https://doi.org/10.1016/j.neuroimage.2013.05.079.
[34] V.D. Calhoun, R. Miller, G. Pearlson, T. Adalı, The chronnectome: time-varying connectivity networks as the next frontier in fMRI data discovery, Neuron 84 (2014) 262–274, https://doi.org/10.1016/j.neuron.2014.10.015.
[35] J.L. Cantero, M. Atienza, A. Cruz-Vadell, A. Suarez-Gonzalez, E. Gil-Neciga, Increased synchronization and decreased neural complexity underlie thalamocortical oscillatory dynamics in mild cognitive impairment, Neuroimage 46 (2009) 938–948, https://doi.org/10.1016/j.neuroimage.2009.03.018.
[36] J. Sun, et al., Complexity analysis of EEG, MEG, and fMRI in mild cognitive impairment and Alzheimer's disease: a review, Entropy 22 (2020) 239, https://doi.org/10.3390/e22020239.
[37] A. Anier, et al., Relationship between approximate entropy and visual inspection of irregularity in the EEG signal, a comparison with spectral entropy, Br. J. Anaesth. 109 (2012) 928–934, https://doi.org/10.1093/bja/aes312.
[38] T. Mizuno, et al., Assessment of EEG dynamical complexity in Alzheimer's disease using multiscale entropy, Clin. Neurophysiol. 121 (2010) 1438–1446, https://doi.org/10.1016/j.clinph.2010.03.025.
[39] B. Song, S. Yoshida, Temporal Graphormer and its interpretability: a novel framework for diagnostic decoding of brain disorders using fMRI data, Biomed. Signal Process. Control 104 (2025) 107467, https://doi.org/10.1016/j.bspc.2024.107467.
[40] V. Rodríguez-González, P. Núñez, C. Gómez, H. Hoshi, Y. Shigihara, R. Hornero, J. Poza, Unveiling the alterations in the frequency-dependent connectivity structure of MEG signals in mild cognitive impairment and Alzheimer's disease, Biomed. Signal Process. Control 87 (2024) 105512, https://doi.org/10.1016/j.bspc.2023.105512.
[41] D.V. Puri, P.H. Kachare, S.L. Nalbalwar, Metaheuristic optimized time–frequency features for enhancing Alzheimer's disease identification, Biomed. Signal Process. Control 94 (2024) 106244, https://doi.org/10.1016/j.bspc.2024.106244.
[42] J.E. Santos Toural, A. Montoya Pedrón, E.J. Marañón Reyes, Classification among healthy, mild cognitive impairment and Alzheimer's disease subjects based on wavelet entropy and relative beta and theta power, Pattern Anal. Appl. 24 (2021) 413–422, https://doi.org/10.1007/s10044-020-00917-5.
[43] J. Li, L. Zhang, H. Meng, P. Li, G. Liu, Analysis of the brain network activity of left- and right-handed persons performing imaginary hand motions, J. Med. Imaging Health Inform. 7 (2017) 1594–1601, https://doi.org/10.1166/jmihi.2017.2171.
[44] K. Yoder, et al., Fractal dimension distributions of resting-state electroencephalography (EEG) improve detection of dementia and Alzheimer's disease compared to traditional fractal analysis, Clin. Transl. Neurosci. 8 (2024) 27, https://doi.org/10.3390/ctn8030027.
[45] A. Al-Nuaimi, E. Jammeh, L. Sun, E. Ifeachor, Complexity measures for quantifying changes in electroencephalogram in Alzheimer's disease, Complexity 2018 (2018) 8915079, https://doi.org/10.1155/2018/8915079.
[46] X. Li, et al., Decreased resting-state brain signal complexity in patients with mild cognitive impairment and Alzheimer's disease: a multi-scale entropy analysis, Biomed. Opt. Express 9 (2018) 1916–1929, https://doi.org/10.1364/BOE.9.001916.
[47] H. Ferdinando, S. Moradi, H. Korhonen, H. Helakari, V. Kiviniemi, T. Myllylä, Spectral entropy provides separation between Alzheimer's disease patients and controls: a study of fNIRS, Eur. Phys. J. Spec. Top. 232 (2023) 655–662, https://doi.org/10.1140/epjs/s11734-022-00753-w.
[48] F.C. Morabito, et al., Network-level permutation entropy of resting-state MEG recordings: a novel biomarker for early-stage Alzheimer's disease? Netw. Neurosci. (2022) 6382–6407, https://doi.org/10.1162/netn_a_00224.
[49] T. Uudeberg, J. Belikov, L. Päeske, H. Hinrikus, I. Liiv, M. Bachmann, In-phase matrix profile: a novel method for the detection of major depressive disorder, Biomed. Signal Process. Control 88 (2024) 105378, https://doi.org/10.1016/j.bspc.2023.105378.
[50] A.B. Das, M.I.H. Bhuiyan, Discrimination and classification of focal and non-focal EEG signals using entropy-based features in the EMD-DWT domain, Biomed. Signal Process. Control 29 (2016) 11–21, https://doi.org/10.1016/j.bspc.2016.05.004.
[51] T. Zhang, Z. Han, X. Chen, W. Chen, Subbands and cumulative sum of subbands based nonlinear features enhance the performance of epileptic seizure detection, Biomed. Signal Process. Control 69 (2021) 102827, https://doi.org/10.1016/j.bspc.2021.102827.
[52] World Medical Association: Declaration of Helsinki: ethical principles for medical research involving human subjects. JAMA 2000;284:3043-3045. https://doi.org/10.1001/jama.284.23.3043.
[53] S. Jahani, S.K. Setarehdan, D.A. Boas, M.A. Yücel, Motion artifact detection and correction in functional near-infrared spectroscopy: a new hybrid method based on spline interpolation method and Savitzky-Golay filtering, Neurophotonics 5 (1) (2018) 015003, https://doi.org/10.1117/1.NPh.5.1.015003.
[54] D. Yang, K.-S. Hong, Quantitative assessment of resting-state for mild cognitive impairment detection: a functional near-infrared spectroscopy and deep learning approach, J. Alzheimers Dis. 80 (2021) 647–663, https://doi.org/10.3233/JAD-201345.
[55] T. Higuchi, Approach to an irregular time series on the basis of the fractal theory, Phys. D 31 (1988) 277–283, https://doi.org/10.1016/0167-2789(88)90081-4.
[56] R. Salazar-Varas, R.A. Vazquez, Evaluating the effect of the cutoff frequencies during the pre-processing stage of motor imagery EEG signals classification, Biomed. Signal Process. Control 54 (2019) 101592, https://doi.org/10.1016/j.bspc.2019.101592.
[57] D.V. Puri, S.L. Nalbalwar, A.B. Nandgaonkar, J.P. Gawande, A. Wagh, Automatic detection of Alzheimer's disease from EEG signals using low-complexity orthogonal wavelet filter banks, Biomed. Signal Process. Control 81 (2023) 104439, https://doi.org/10.1016/j.bspc.2022.104439.
[58] J. Wanliss, G.E. Wanliss, Efficient calculation of fractal properties via the Higuchi method, Nonlinear Dyn. 109 (2022) 2893–2900, https://doi.org/10.1007/s11071-022-07608-x.
[59] T. Inouye, K. Shinosaki, H. Sakamoto, S. Toi, S. Ukai, A. Iyama, Y. Katsuda, M. Hirano, Quantification of EEG irregularity by use of the entropy of the power spectrum, Electroencephalogr. Clin. Neurophysiol. 79 (1991) 204–210, https://doi.org/10.1016/0013-4694(91)90146-5.
[60] Z. Gao, Y. Cui, F. Wan, Y. Yang, Y. Liu, Relative wavelet entropy complex network for improving EEG-based fatigue driving classification, IEEE Trans. Instrum. Meas. 68 (2019) 2491–2497, https://doi.org/10.1109/TIM.2018.2865842.
[61] A. Tzabazis, A. Eisenried, D.C. Yeomans, M.I.V. Hyatt, Wavelet analysis of heart rate variability: Impact of wavelet selection, Biomed. Signal Process. Control 40 (2018) 220–225, https://doi.org/10.1016/j.bspc.2017.09.027.
[62] S.S. Shapiro, M.B. Wilk, An analysis of variance test for normality (complete samples), Biometrika 52 (1965) 591–611, https://doi.org/10.1093/biomet/52.3-4.591.
[63] Z. Šidák, Rectangular confidence regions for the means of multivariate normal distributions, J. Am. Stat. Assoc. 62 (1967) 626–633, https://doi.org/10.2307/2283989.
[64] M. Banerjee, E. Reynolds, H.B. Andersson, B.K. Nallamothu, Tree-Based Analysis. Circ. Cardiovasc. Qual. Outcomes 12 (5) (2019) e004879, https://doi.org/10.1161/CIRCOUTCOMES.118.004879.
[65] Z. Pu, H. Huang, M. Li, H. Li, X. Shen, Q. Wu, Q. Ni, Y. Lin, D. Cui, An exploration of distinguishing subjective cognitive decline and mild cognitive impairment based on resting-state prefrontal functional connectivity assessed by functional near-infrared spectroscopy, Front. Aging Neurosci. 16 (2025) 1468246, https://doi.org/10.3389/fnagi.2024.1468246.
[66] Y. Zhou, H. Xie, X. Li, et al., Predicting upper limb motor recovery in subacute stroke patients via fNIRS-measured cerebral functional responses induced by robotic training, J. Neuroeng. Rehabil. 21 (1) (2024) 226, https://doi.org/10.1186/s12984-024-01523-6.
[67] E.R. DeLong, D.M. DeLong, D.L. Clarke-Pearson, Comparing the areas under two or more correlated receiver operating characteristic curves: a nonparametric approach, Biometrics 44 (1988) 837–845, https://doi.org/10.2307/2531595.
[68] J. Subramanian, J. Savage, M. Tremblay, Synaptic loss in Alzheimer's disease: mechanistic insights provided by two-photon in vivo imaging of transgenic mouse models, Front. Cell. Neurosci. 14 (2020) 592607, https://doi.org/10.3389/fncel.2020.592607.
[69] R. Zhang, et al., A longitudinal study of functional brain complexity in progressive Alzheimer's disease, Alzheimers Dement. Diagn. Assess. Dis. Monit. 17 (2025) e70059, https://doi.org/10.1002/dad2.70059.
[70] P. Ren, M. Ma, G. Xie, Z. Wu, D. Wu, Alzheimer's Disease Neuroimaging Initiative: Altered complexity of resting-state BOLD activity in Alzheimer's disease-related neurodegeneration: a multiscale entropy analysis, Aging (Albany NY) 12 (2020) 13571–13582. https://doi.org/10.18632/aging.103463.
[71] L. Fu, et al., Functional abnormality associated with tau deposition in Alzheimer's disease – a hybrid positron emission tomography/MRI study, Front. Aging Neurosci. 13 (2021) 758053, https://doi.org/10.3389/fnagi.2021.758053.
[72] J. Choi, et al., Prefrontal EEG slowing, synchronization, and ERP peak latency in association with predementia stages of Alzheimer's disease, Front. Aging Neurosci. 15 (2023) 1131857, https://doi.org/10.3389/fnagi.2023.1131857.
[73] Y. Hu, T. Zhu, W. Zhang, Alzheimer's Disease Neuroimaging Initiative: the characteristics of brain atrophy prior to the onset of Alzheimer's disease: a longitudinal study, Front. Aging Neurosci. 16 (2024) 1344920, https://doi.org/10.3389/fnagi.2024.1344920.
[74] R.J. Melrose, A.M. Jimenez, H. Riskin-Jones, G. Weissberger, J. Veliz, A. S. Hasratian, S. Wilkins, D.L. Sultzer, Alterations to task positive and task negative networks during executive functioning in mild cognitive impairment, NeuroImage Clin. 19 (2018) 970–981, https://doi.org/10.1016/j.nicl.2018.06.014.
[75] P. Liang, Z. Wang, Y. Yang, X. Jia, K. Li, Functional disconnection and compensation in mild cognitive impairment: evidence from DLPFC connectivity using resting-state fMRI, PLoS One 6 (2011) e22153, https://doi.org/10.1371/journal.pone.0022153.
[76] Y. Zhang, L. Simon-Vermot, M.Á. Araque Caballero, B. Gesierich, A.N.W. Taylor, M. Duering, M. Dichgans, M. Ewers, Alzheimer's Disease Neuroimaging Initiative: Enhanced resting-state functional connectivity between core memory-task activation peaks is associated with memory impairment in MCI, Neurobiol. Aging 45 (2016) 43–49, https://doi.org/10.1016/j.neurobiolaging.2016.04.018.
[77] M. Li, et al., Alterations in resting-state functional connectivity of the default mode network in amnestic mild cognitive impairment: an fMRI study, BMC Med. Imaging 17 (2017) 48, https://doi.org/10.1186/s12880-017-0221-9.
[78] W. Xu, S. Chen, C. Xue, G. Hu, W. Ma, W. Qi, X. Lin, J. Chen, Functional MRI-specific alterations in executive control network in mild cognitive impairment: an ALE meta-analysis, Front. Aging Neurosci. 12 (2020) 578863, https://doi.org/10.3389/fnagi.2020.578863.
[79] Z. Pu, H. Huang, M. Li, H. Li, X. Shen, L. Du, Q. Wu, X. Fang, X. Meng, Q. Ni, G. Li, D. Cui, Screening tools for subjective cognitive decline and mild cognitive impairment based on task-state prefrontal functional connectivity: a functional

near-infrared spectroscopy study, Neuroimage 310 (2025) 121130, https://doi.org/10.1016/j.neuroimage.2025.121130.
[80] Y. Diao, H. Wang, X. Wang, et al., Discriminative analysis of schizophrenia and major depressive disorder using fNIRS, J. Affect. Disord. 361 (2024) 256–267, https://doi.org/10.1016/j.jad.2024.06.013.
[81] G. Ma, A.E. Eng, S.K. Chiang, et al., A comparative diagnostic study using clinical and multimodal assessment, including functional neuroimaging and oculomotricity tools, to differentiate ADHD in young patients from healthy control group, Psychiatry Clin. Neurosci. 79 (4) (2025) 165–175, https://doi.org/10.1111/pcn.13788.
[82] Q. Shi, J. Zhong, L. Zhang, H. Liu, J. Li, H. Peng, B. Hu, Robust semi-supervised extraction of information using functional near-infrared spectroscopy for diagnosing depression, Biomed. Signal Process. Control 105 (2025) 107571, https://doi.org/10.1016/j.bspc.2025.107571.
[83] J. Zhong, Z. Shan, X. Zhang, H. Lu, H. Peng, B. Hu, Robust discriminant feature extraction for automatic depression recognition, Biomed. Signal Process. Control 82 (2023) 104505, https://doi.org/10.1016/j.bspc.2022.104505.
[84] S. Maddury, The performance of domain-based feature extraction on EEG, ECG, and fNIRS for Huntington's disease diagnosis via shallow machine learning, Front. Signal Process. 4 (2024) 1321861, https://doi.org/10.3389/frsip.2024.1321861.